SUPPORTING INFORMATION

Degradation Mechanism of Vanadium Oxide-Based Aqueous Zinc-Ion Batteries

Gongzheng Yang[1], Qian Li[1], Kaixuan Ma[1], Cheng Hong[1], Chengxin Wang[1,2]*

[1]*State Key Laboratory of Optoelectronic Materials and Technologies, School of Materials Science and Engineering, Sun Yat-sen (Zhongshan) University, Guangzhou 510275, People's Republic of China*

[2]*The Key Laboratory of Low-carbon Chemistry & Energy Conservation of Guangdong Province, Sun Yat-sen (Zhongshan) University, Guangzhou 510275, People's Republic of China*

*Correspondence and requests for materials should be addressed to C. X. Wang.

Tel & Fax: +86-20-84113901

E-mail: wchengx@mail.sysu.edu.cn

EXPERIMENTAL SECTION

Materials Synthesis.

$H_{11}Al_2V_6O_{23.2}$: A facile hydrothermal method is employed to the synthesis of $H_{11}Al_2V_6O_{23.2}$. In a typical procedure, 585 mg ammonium vanadate (NH_4VO_3) powders are added into 97 mL deionized water and are stirred to a faint yellow solution under heating at 80 ^oC. Then, 3 mL 1 mol L^{-1} hydrochloric acid (HCl) is dropped in the solution. After stirring for 10 minutes, 1207 mg crystalline aluminum chloride ($AlCl_3 \cdot 6H_2O$) powders are added into the solution. Subsequently, the obtained yellow dispersion is poured into a Teflon-lined autoclave and heated to 150 ^oC for 6 hours. Finally, the precipitate in the bottom of vessel is collected, followed with washing by deionized water and absolute alcohol three times, and dried in air at 60 ^oC for 12 hours.

VO_2: The fabrication of VO_2 adopts the same method reported by Ding et al. Firstly, 1.5 g vanadium pentoxide (V_2O_5) and 2.25 g oxalic acid dihydrate ($H_2C_2O_4 \cdot 2H_2O$) powders are added into 100 mL deionized water and the mixture is heated at 80 ^oC for 6 hours. Then, the obtained dispersion is transferred into a Teflon-lined autoclave and heated to 180 ^oC for 12 hours. Finally, the precipitate in the bottom of vessel is collected, followed with washing by deionized water and absolute alcohol three times, and dried in air at 60 ^oC for 12 hours.

$V_5O_{12} \cdot 6H_2O$: A sol-gel method is adopted to fabricate the $V_5O_{12} \cdot 6H_2O$ sheets, which has been reported in our previous work. In a typical synthesis, 4 g V_2O_5 is heated in a muffle furnace at 900 ^oC to obtain a molten oxide. Then, the molten oxide is quickly poured into 100 mL deionized water under stirring. After aging for 48 hours, a homogenous brick red gel is obtained and subsequently freezes drying to get $V_5O_{12} \cdot 6H_2O$.

V_2O_5: The V_2O_5 is prepared by heating the $V_5O_{12} \cdot 6H_2O$ in air at 500 ^oC for 2 hours.

$K_{0.486}V_2O_5$: In a typical synthesis of $K_{0.486}V_2O_5$, 585 mg NH_4VO_3 powders are added into 99 mL deionized water and are stirred to a faint yellow solution under heating at 80 ^oC. Then, 1 mL 1 mol L^{-1} 1HCl is dropped in the solution. After stirring for 10 minutes, 138 mg potassium metavanadate (KVO_3) powders are dissolved into the

solution. Subsequently, the obtained dark green dispersion is poured into a Teflon-lined autoclave and heated to 180 ^{o}C for 12 hours. Finally, the precipitate in the bottom of vessel is collected, followed with washing by deionized water and absolute alcohol three times, and dried in air at 60 ^{o}C for 12 hours.

Materials characterizations. X-ray diffraction (XRD) measurements (Rigaku Co., Japan, Cu Kα radiation, working voltage of 40 kV) are employed to examine the crystal structure. The morphologies and microstructures are detected by scanning electron microscope (SEM, JEOL, 15kV) and transmission electron microscopy (TEM, FEI Tecnai G2 F30, 300 kV) attached with energy dispersive spectroscopy (EDS), respectively. X-ray photoelectron spectroscopy (XPS) studies are carried out on PerkinElmer PHI 1600 ESCA. Raman spectra are recorded from a Renishaw INVIA micro-Raman spectroscopy system.

Electrochemical tests. A CR2032 coin-type cell is fabricated to evaluate the electrochemical properties of materials. A metallic Zn foil with a diameter of 14 mm, a glass fiber (GF/A, Whatman) with a diameter of 16 mm, and an aqueous 2 mol L^{-1} $Zn(ClO_4)_2$ solution, are introduced as counter/reference electrode, separator, and electrolyte, respectively. The cathode is prepared by mixing 70 wt% active materials (such as $H_{11}Al_2V_6O_{23.2}$, VO_2, $V_5O_{12}{\cdot}6H_2O$, V_2O_5, $K_{0.486}V_2O_5$), 20 wt% conductive agent (Super P), and 10 wt% polyvinylidene fluoride (PVDF) in N-methyl-2-pyrrolidone solvent. Then, the homogenous dispersed slurry is pasted on a graphite paper, heated at 80 ^{o}C overnight, and finally cut into disks with a diameter of 12 mm. The mass loading of the active materials is 1.5 mg cm^{-2}. Cyclic voltammerty (CV) is tested on an Autolab potentiaostat in a voltage window of 0.3 – 1.6 V for $H_{11}Al_2V_6O_{23.2}$, VO_2, V_2O_5, and $K_{0.486}V_2O_5$, and 0.4 – 1.6 V for $V_5O_{12}{\cdot}6H_2O$, respectively. The charge/discharge tests are carried out using the battery testers (NEWARE, Shenzhen) at various currents. To better study the electrochemical mechanism, the active materials are loaded on titanium foil with a thickness of 20 μm.

Table S1. Summary of the cycling performance of representative vanadium oxides in ARZIBs.

Material	**Electrolyte**	**Specific capacity** (Capacity/Current)	**Cycling performance** (Current Cycle number/ Capacity retention)		**Byproduct**	**Ref.**
			Low Current	**High Current**		
$Zn_{0.25}V_2O_5{\cdot}nH_2O$	1 M $ZnSO_4$	300 mAh g^{-1} 50 mA g^{-1}	/	2400 mA g^{-1} 1000 / 81%	/	1
$V_{1-x}Al_xO_{1.52}(OH)_{0.77}$	1 M $ZnSO_4$	156 mAh g^{-1} 15 mA g^{-1}	15 mA g^{-1} 50 / 67.3%	/	ZHS ZVO	2
V_2O_5	1 M $Zn(CF_3SO_3)_2$ 21 M LITFSI	238 mAh g^{-1} 50 mA g^{-1}	100 mA g^{-1} 160 / 95%	2000 mA g^{-1} 2000 / 80%	/	3
$V_2O_5{\cdot}nH_2O$	3 M $Zn(CF_3SO_3)_2$	381 mAh g^{-1} 60 mA g^{-1}	/	6000 mA g^{-1} 900 / 71%	/	4
$H_2V_3O_8$	3 M $Zn(CF_3SO_3)_2$	423.8 mAh g^{-1} 100 mA g^{-1}	/	5000 mA g^{-1} 1000 / 94.3%	/	5
$Zn_2V_2O_7$	1 M $ZnSO_4$	248 mAh g^{-1} 50 mA g^{-1}	/	4000 mA g^{-1} 1000 / 85%	ZHS	6
$Zn_3V_2O_7(OH)_2{\cdot}2H_2O$	1 M $ZnSO_4$	213 mAh g^{-1} 50 mA g^{-1}	/	200 mA g^{-1} 300 / 68%	ZHS	7
$Na_2V_6O_{16}{\cdot}3H_2O$	1 M $ZnSO_4$	361 mAh g^{-1} 100 mA g^{-1}	/	14440 mA g^{-1} 1000 / 84.5%	ZHS	8
$Ca_{0.24}V_2O_5{\cdot}0.83H_2O$	1 M $ZnSO_4$	340 mAh g^{-1} 57.8 mA g^{-1}	/	23120 mA g^{-1} 3000 / 96%	/	9
$Na_{0.33}V_2O_5$	3 M $Zn(CF_3SO_3)_2$	367.1 mAh g^{-1} 100 mA g^{-1}	/	1000 mA g^{-1} 1000 / 93%	/	10
VO_2	3 M $Zn(CF_3SO_3)_2$	274 mAh g^{-1} 100 mA g^{-1}	/	10000 mA g^{-1} 10000 / 79%	/	11

VO_2	3 м $Zn(CF_3SO_3)_2$	357 mAh g^{-1} 100 mA g^{-1}	100 mA g^{-1} 50 / 100%	2000 mA g^{-1} 300 / 91.2%	/	12
$Na_2V_6O_{16}·1.63H_2O$	3 м $Zn(CF_3SO_3)_2$	357 mAh g^{-1} 50 mA g^{-1}	100 mA g^{-1} 100 / 72%	5000 mA g^{-1} 6000 / 90%	/	13
$Na_{1.1}V_3O_{7.9}$	1 м $Zn(CF_3SO_3)_2$	238 mAh g^{-1} 50 mA g^{-1}	/	300 mA g^{-1} 100 / 76.7%	/	14
$K_2V_8O_{21}$	2 м $ZnSO_4$	247 mAh g^{-1} 300 mA g^{-1}	/	6000 mA g^{-1} 300 / 83%	ZVO	15
$Na_5V_{12}O_{32}$	2 м $ZnSO_4$	281 mAh g^{-1} 500 mA g^{-1}	/	4000 mA g^{-1} 2000 / 71%	/	16
$Mg_{0.34}V_2O_5·0.84H_2O$	3 м $Zn(CF_3SO_3)_2$	353 mAh g^{-1} 100 mA g^{-1}	100 mA g^{-1} 200 / 100%	5000 mA g^{-1} 2000 / 97%	/	17
VO_2/rGO	1 м $ZnSO_4$	365 mAh g^{-1} 50 mA g^{-1}	50 mA g^{-1} 200 / 80%	1750 mA g^{-1} 2000 / 97%	ZHS	18
$NH_4V_4O_{10}$	3 м $Zn(CF_3SO_3)_2$	147 mAh g^{-1} 200 mA g^{-1}	/	5000 mA g^{-1} 5000 / 70.3%	/	19
$Li_xV_2O_5·nH_2O$	2 м $ZnSO_4$	470 mAh g^{-1} 500 mA g^{-1}	/	10000 mA g^{-1} 1000 / 63%	/	20
$NaV_3O_8·1.5H_2O$	1 м $ZnSO_4$ 1 м Na_2SO_4	380 mAh g^{-1} 50 mA g^{-1}	/	4000 mA g^{-1} 1000 / 82%	ZHS	21
V^{4+}-V_2O_5	2 м $ZnSO_4$	262.1 mAh g^{-1} 1000 mA g^{-1}	/	10000 mA g^{-1} 1000 / 74%	ZHS	22
VO_2/rGO	3 м $Zn(CF_3SO_3)_2$	276 mAh g^{-1} 100 mA g^{-1}	/	4000 mA g^{-1} 1000 / 99%	/	23
$(NH_4)_2V_{10}O_{25}·8H_2O$	2 м $ZnSO_4$	376 mAh g^{-1} 500 mA g^{-1}	/	4000 mA g^{-1} 1000 / 93%	ZVO	24
$V_5O_{12}·6H_2O$	3 м $Zn(CF_3SO_3)_2$	354.8 mAh g^{-1} 500 mA g^{-1}	/	2000 mA g^{-1} 1000 / 94%	/	25
NaV_6O_{15}	1 м $ZnSO_4$	427 mAh g^{-1}	/	1000 mA g^{-1}	ZHS	26

		50 mA g^{-1}		300 / 83%		
V_6O_{13}	3 м $Zn(CF_3SO_3)_2$	360 mAh g^{-1} 200 mA g^{-1}	/	4000 mA g^{-1} 2000 / 92%	/	27
$Ag_{0.33}V_2O_5$	3 м $Zn(CF_3SO_3)_2$	448 mAh g^{-1} 200 mA g^{-1}	/	3000 mA g^{-1} 700 / 35.6%	/	28
VO_2	1 м $ZnSO_4$	353 mAh g^{-1} 1000 mA g^{-1}	/	3000 mA g^{-1} 945 / 75.5%	ZHS	29
V_6O_{13}	3 м $ZnSO_4$	450 mAh g^{-1} 100 mA g^{-1}	/	10000 mA g^{-1} 3000 / 74.9%	/	30
$(NH_4)_{0.5}V_2O_5$	2 м $ZnSO_4$	418.4 mAh g^{-1} 100 mA g^{-1}	/	5000 mA g^{-1} 2000 / 91.4%	ZHS	31
$V_{10}O_{24}{\cdot}12H_2O$	3 м $Zn(CF_3SO_3)_2$	415 mAh g^{-1} 100 mA g^{-1}	/	5000 mA g^{-1} 3000 / 98%	/	32
$Cu_{0.1}V_2O_5{\cdot}0.08H_2O$	2 м $ZnSO_4$	410 mAh g^{-1} 500 mA g^{-1}	/	10000 mA g^{-1} 10000 / 58.6%	ZVO	33
$MnV_{12}O_{31}{\cdot}10H_2O$	3 м $Zn(CF_3SO_3)_2$	415 mAh g^{-1} 50 mA g^{-1}	/	4000 mA g^{-1} 2000 / 96%	/	34
VO_2	3 м $ZnSO_4$	408 mAh g^{-1} 100 mA g^{-1}	/	15000 mA g^{-1} 20000 / 48.3%	ZHS	35
$V_5O_{12}{\cdot}6H_2O$	3 м $Zn(ClO_4)_2$	496 mAh g^{-1} 100 mA g^{-1}	/	10000 mA g^{-1} 10000 / 84.7%	$Zn_4ClO_4(OH)_7$	36
$V_2O_5{\cdot}2.2H_2O$	Gelatin/ $Zn(CF_3SO_3)_2$	450 mAh g^{-1} 100 mA g^{-1}	/	5000 mA g^{-1} 3000 / 72%	/	37
$NaCa_{0.6}V_6O_{16}{\cdot}3H_2O$	3 м $Zn(CF_3SO_3)_2$	347 mAh g^{-1} 100 mA g^{-1}	/	5000 mA g^{-1} 10000 / 83%	/	38
V_2O_5	Nafion membrane soaked in $ZnSO_4$	510 mAh g^{-1} 250 mA g^{-1}	/	10000 mA g^{-1} 1800 / 88%	/	39
$Ag_{0.333}V_2O_5$@ $V_2O_5{\cdot}nH_2O$	3 м $Zn(CF_3SO_3)_2$	373.3 mAh g^{-1} 200 mA g^{-1}	/	500 mA g^{-1} 100 / 90.1%	/	40

V_2O_5	3 м $Zn(CF_3SO_3)_2$	449.8 mAh g^{-1} 100 mA g^{-1}	/	2000 mA g^{-1} 2000 / 86.8%	/	41
$Zn_{0.3}V_2O_5{\cdot}1.5H_2O$	3 м $Zn(CF_3SO_3)_2$	426 mAh g^{-1} 200 mA g^{-1}	/	10000 mA g^{-1} 20000 / 96%	$Zn_x(OTf)_y(OH)_{2x-y}{\cdot}nH_2O$	42
CuV_2O_6	3 м $Zn(CF_3SO_3)_2$	427 mAh g^{-1} 100 mA g^{-1}	/	5000 mA g^{-1} 3000 / 99.3%	$Zn_x(OH)_y(CF_3SO_3){\cdot}nH_2O$	43
V_2O_5	3 м $Zn(CF_3SO_3)_2$	319 mAh g^{-1} 20 mA g^{-1}	/	588 mA g^{-1} 500 / 81%	ZVO	44
V_2O_5	3 м $Zn(CF_3SO_3)_2$	452 mAh g^{-1} 100 mA g^{-1}	/	588 mA g^{-1} 5000 / 92%	/	45
V_6O_{13}	3 м $Zn(CF_3SO_3)_2$	410 mAh g^{-1} 200 mA g^{-1}	/	2000 mA g^{-1} 2000 / 86%	/	46
$(NH_4)_2V_6O_{16}{\cdot}1.5H_2O$	3 м $Zn(CF_3SO_3)_2$	385 mAh g^{-1} 100 mA g^{-1}	/	8000 mA g^{-1} 10000 / 74.8%	/	47
$Ag_2V_4O_{11}$	3 м $Zn(CF_3SO_3)_2$	213 mAh g^{-1} 200 mA g^{-1}	/	5000 mA g^{-1} 6000 / 93%	$Zn_{12}(CF_3SO_3)_9(OH)_{15}{\cdot}nH_2O$	48
$Zn_3V_2O_7(OH)_2{\cdot}2H_2O$	1 м $ZnSO_4$	227 mAh g^{-1} 100 mA g^{-1}	100 mA g^{-1} 100 / 90%	10000 mA g^{-1} 1000 / 84%	ZHS	49

The low currents means that the applied current density is less than or equal to 100 mA g^{-1}.

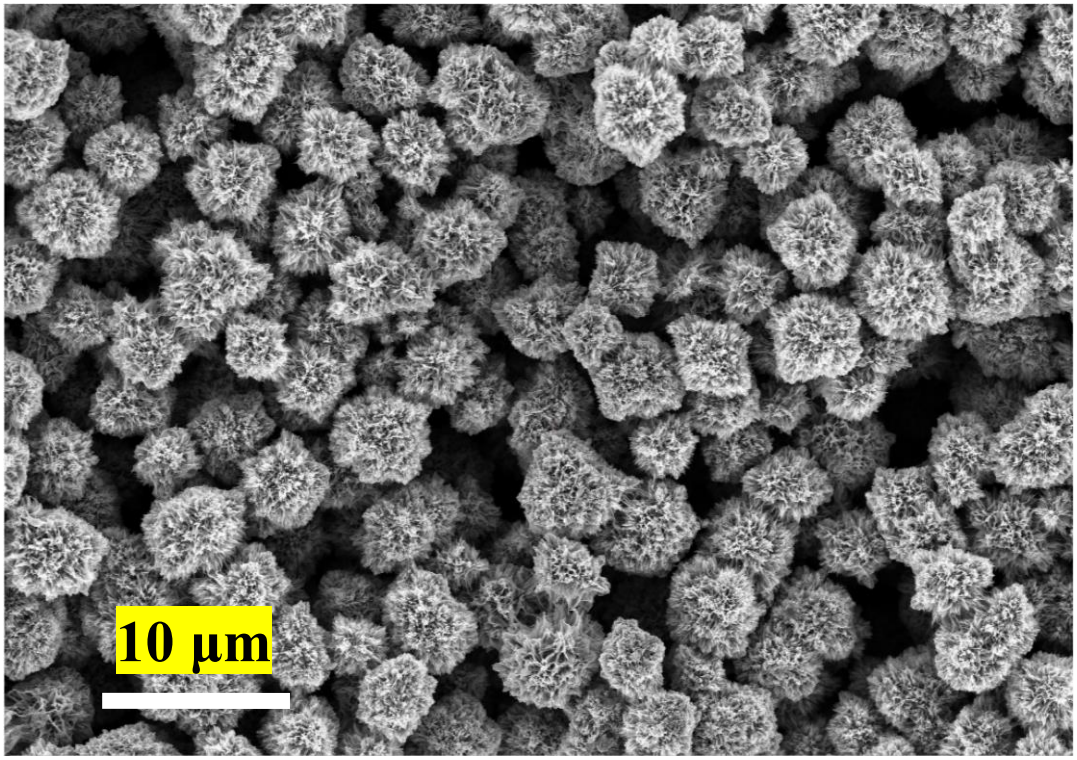

Figure S1. SEM image of the $H_{11}Al_2V_6O_{23.2}$ samples. The SEM image show uniform sphere-like particle with diameter of ~ 5 µm.

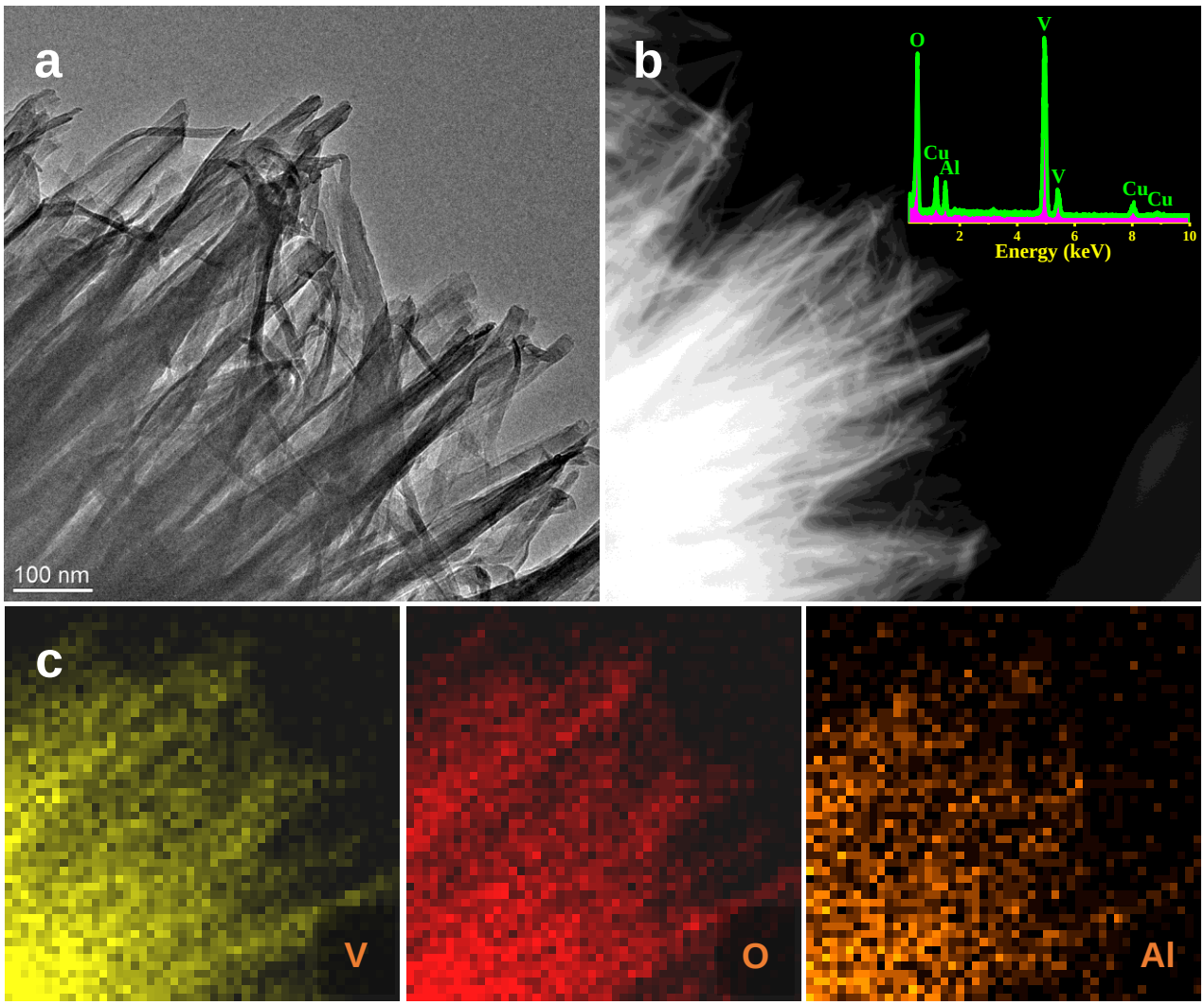

Figure S2. a) TEM, b) STEM, c) EDS-mapping images of the $H_{11}Al_2V_6O_{23.2}$ samples. Inset in b) is the EDS pattern. It can be clearly observed that the sphere-like particles are composed of the self-assembly of nanobelts with a width of less than 20 nm. Combined with STEM observation, the V, O, and Al element mapping images further highlight a high purity of the obtained samples.

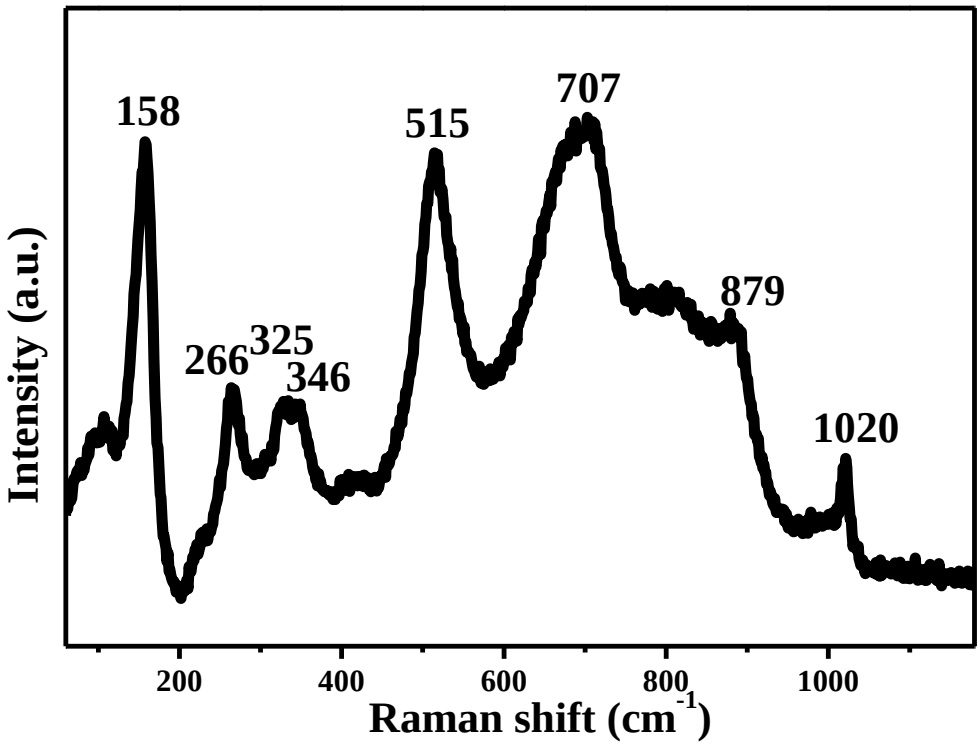

Figure S3. Raman spectra of the $H_{11}Al_2V_6O_{23.2}$ samples. The presented Raman spectra of obtained samples are similar to those in previously reported layered vanadium oxides. The low-wavenumber peak at 158 cm–1 is usually ascribed to the bending vibration of the skeleton, while the high-frequency peaks at 266, 346, 515, 707, 879, and 1020 cm–1 are attributed to the bending vibrations of the O-V-O, V-O, and V-O-V bonds and the stretching vibration of the V-O bonds, respectively.

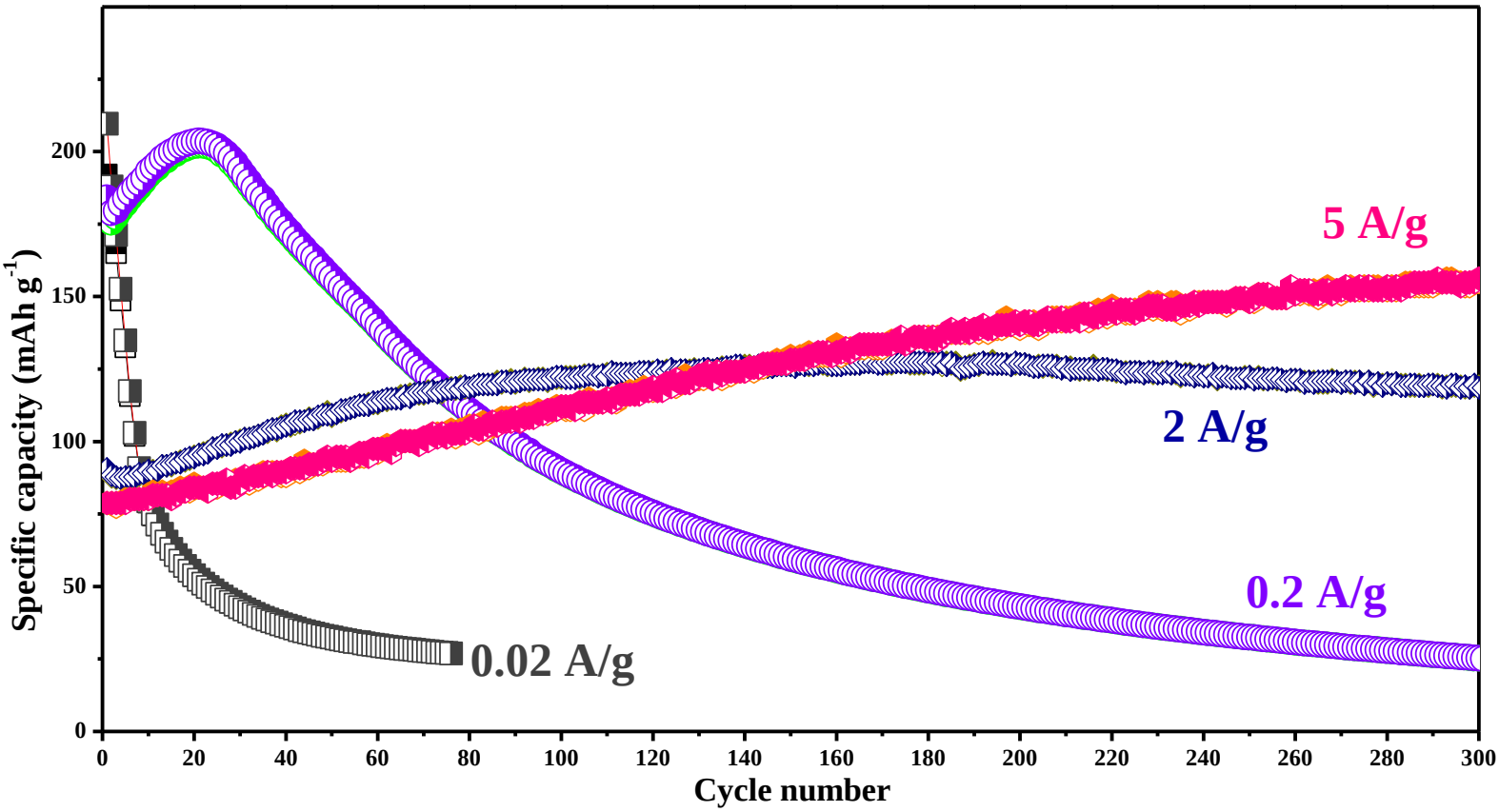

Figure S4. Cycle performances of the $H_{11}Al_2V_6O_{23.2}$ electrodes in the initial 300 cycles collected at different current densities of 0.02, 0.2, 2, and 5 A g^{-1}, respectively. At the lowest rate, the specific capacity of electrodes is dropping rapidly since the first cycle and falls down to the bottom at about 60 cycles. A sharp rise and decline is observed before and after 21 cycles at the current density of 0.2 A g^{-1}. For the cycle performance at 2 A g^{-1}, a slight decrease in the first several cycles, then a creeping increase between 10^{th} to 195^{th} cycle, and finally falling slowly since the 196^{th} cycle are detected. The values obtained at 5 A g^{-1} increase constantly. All of these manifest the different electrochemical behaviors of electrode materials at the low (0.02 and 0.2 A g^{-1}) and high (2 and 5 A g^{-1}) current densities.

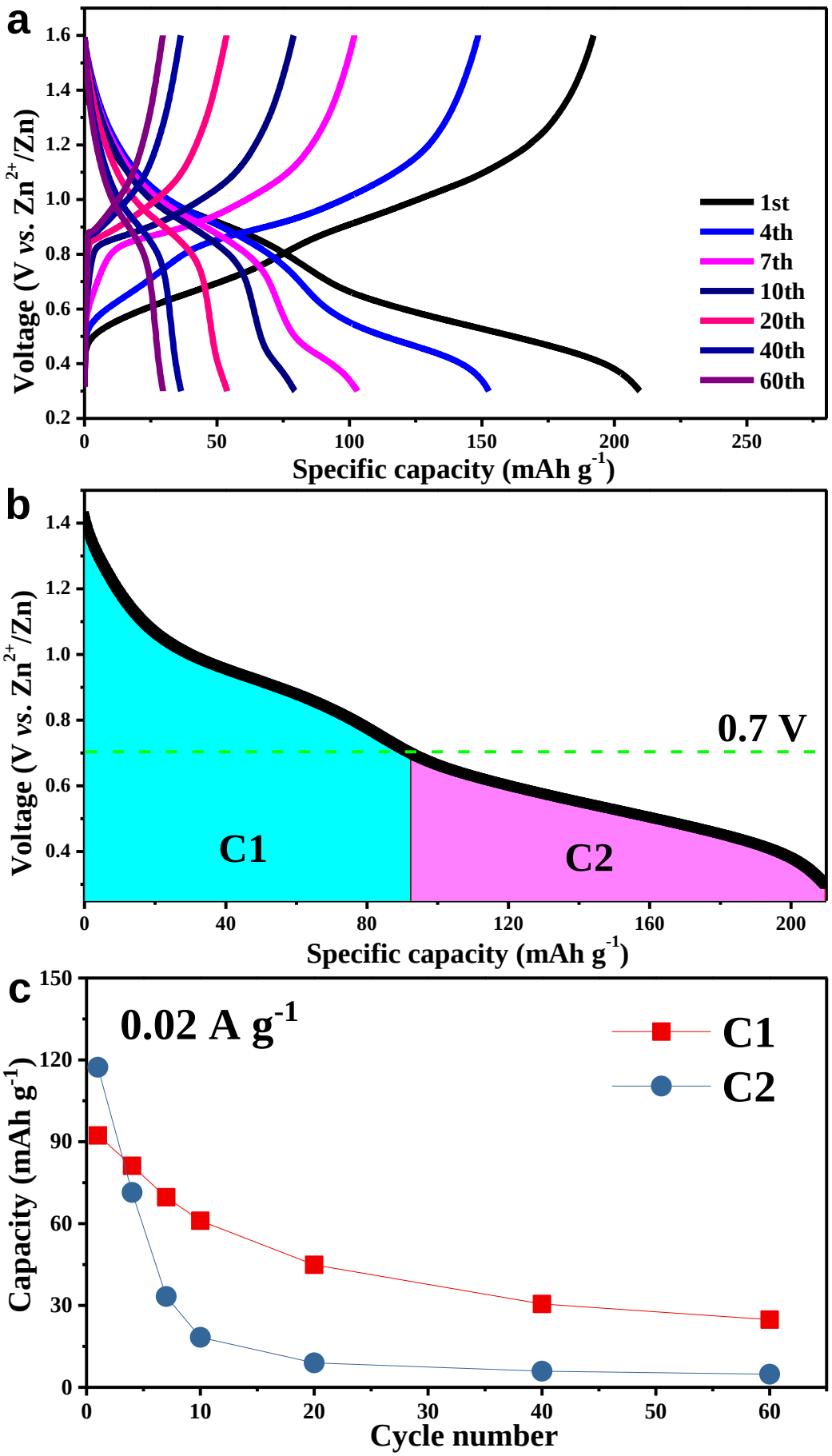

Figure S5. a) Charge/discharge profiles of the $H_{11}Al_2V_6O_{23.2}$ electrodes at a current density of 0.02 A g^{-1} in the different cycles. b) Two parts in the discharge profile with a dividing voltage of 0.7 V. c) The specific capacities of the two parts marked in b.

Shown in Figure S5a, in addition to the rapid decreased specific capacities, it is noteworthy that the discharge capacity obtained at the voltage lower than 0.7 V (0.7 – 0.3 V) in each cycle attenuates much faster than that obtained at the voltage higher than 0.7 V (1.6 – 0.7 V). Taking the cycle number as the abscissa, the specific capacities of the two parts (C2 and C1) for spot and line image in Figure S5c depicts nearly the same trend with the cycling stability in Figure S4. The same phenomenon is also observed as the $H_{11}Al_2V_6O_{23.2}$ electrodes measured at 0.2, 2, and 5 A g^{-1}, respectively, which are illustrated in Figure S6-8. In order to clarify these interesting results, the following question must be well addressed: what is the electrochemical reaction mechanism of $H_{11}Al_2V_6O_{23.2}$ as cathode material for aqueous zinc-ion batteries?

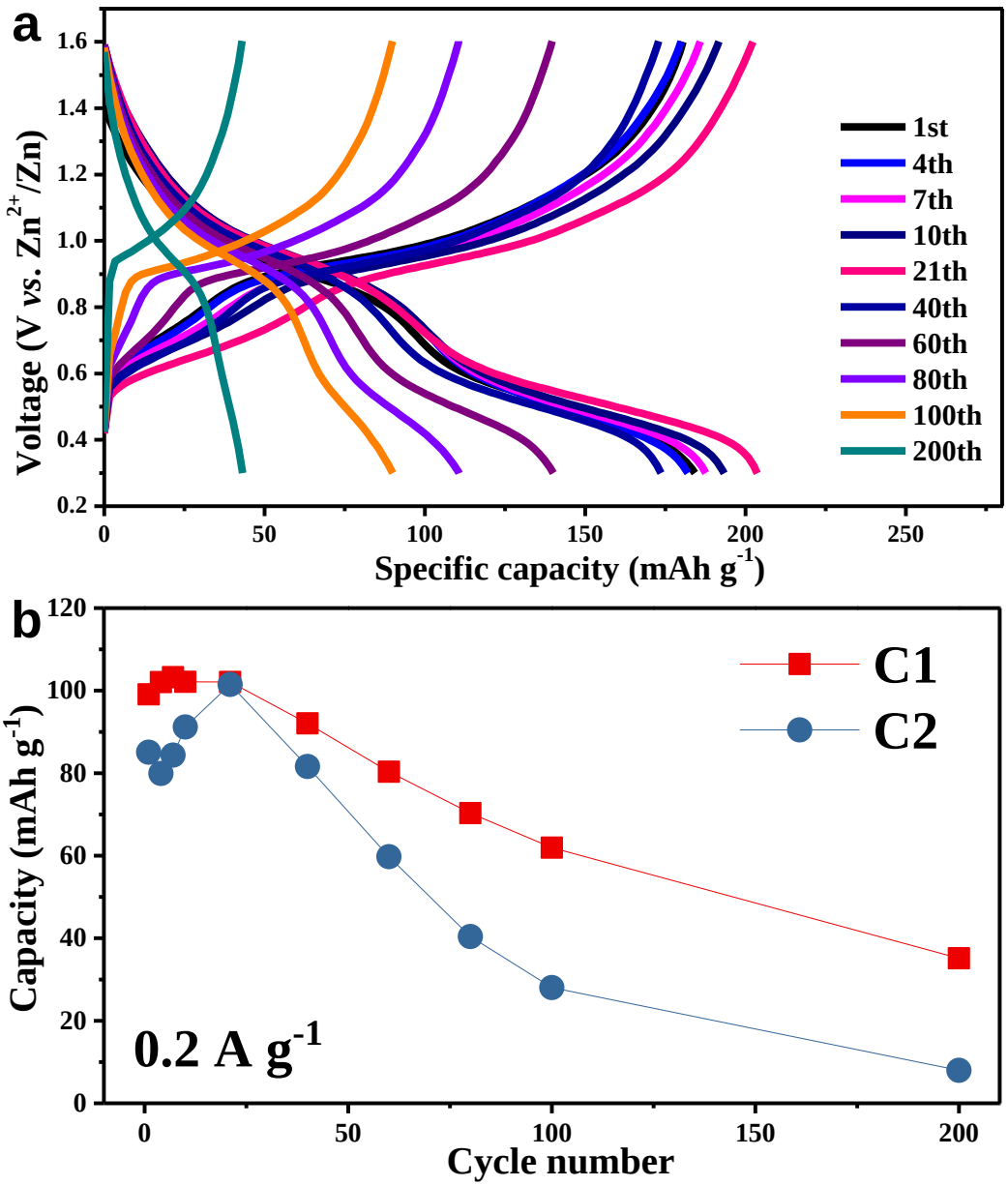

Figure S6. a) Charge/discharge profiles of the $H_{11}Al_2V_6O_{23.2}$ electrodes at a current density of 0.2 A g^{-1} in the different cycles. b) The specific capacities of C1 and C2.

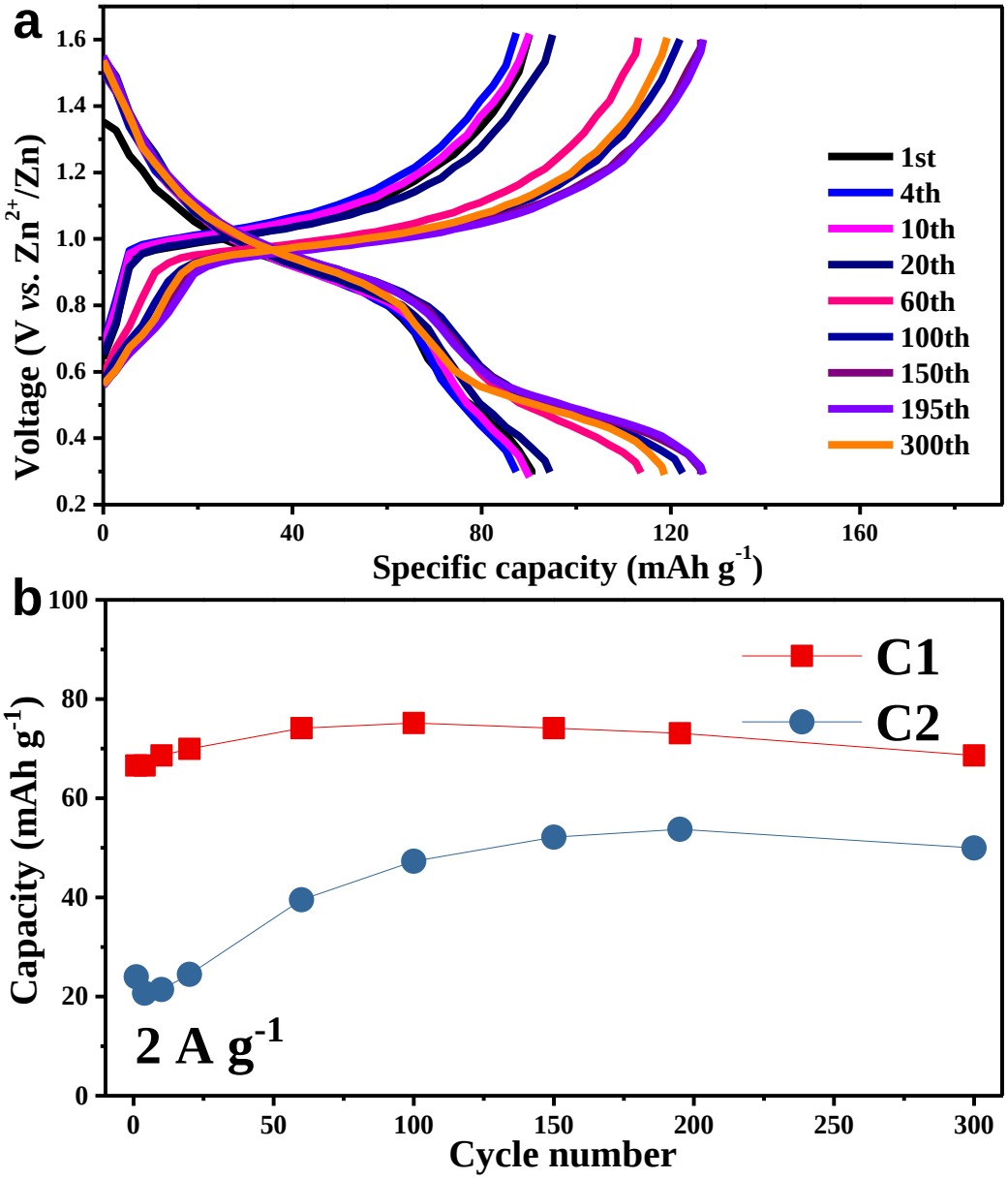

Figure S7. a) Charge/discharge profiles of the $H_{11}Al_2V_6O_{23.2}$ electrodes at a current density of 2 A g^{-1} in the different cycles. b) The specific capacities of C1 and C2.

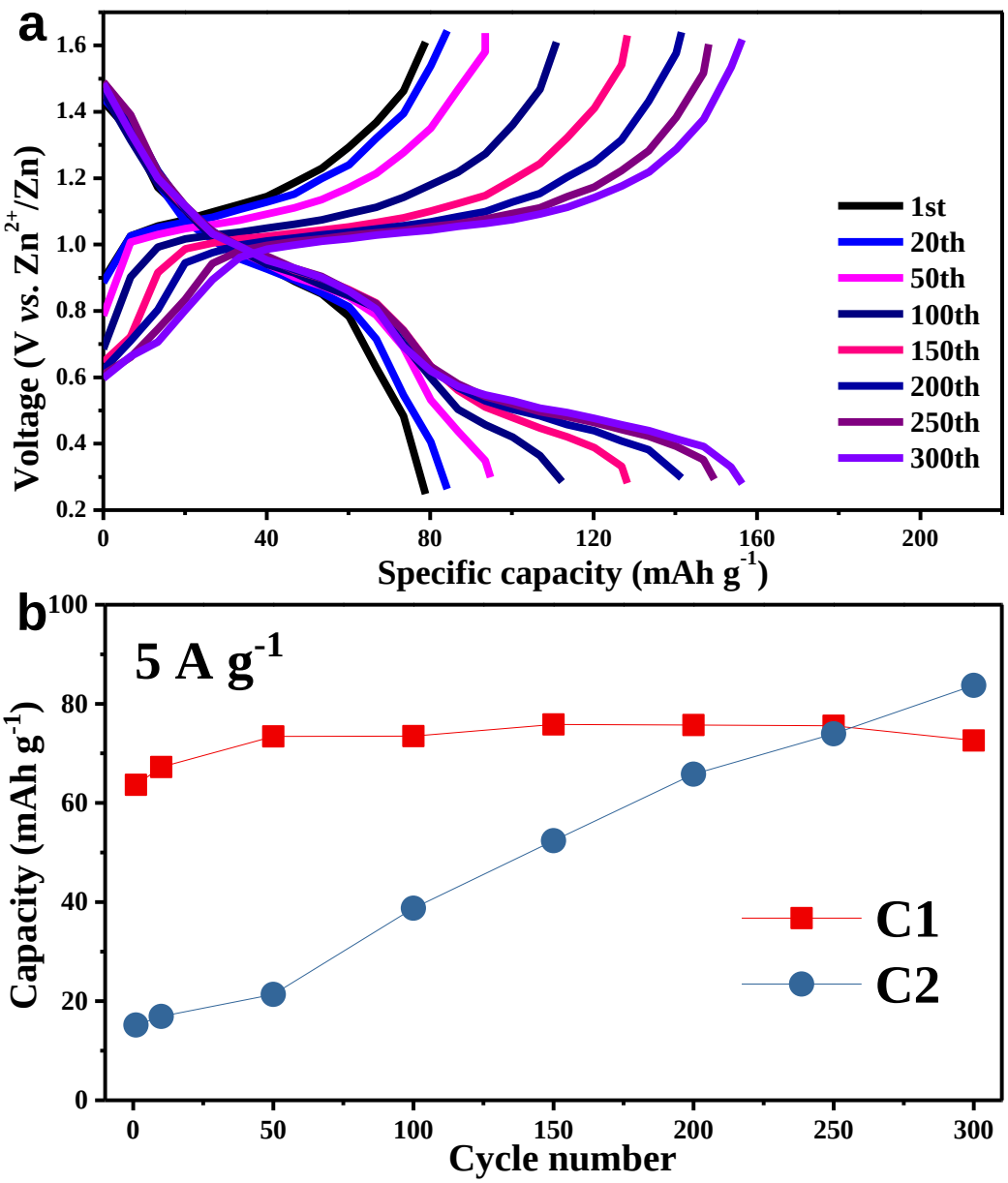

Figure S8. a) Charge/discharge profiles of the $H_{11}Al_2V_6O_{23.2}$ electrodes at a current density of 5 A g^{-1} in the different cycles. b) The specific capacities of C1 and C2.

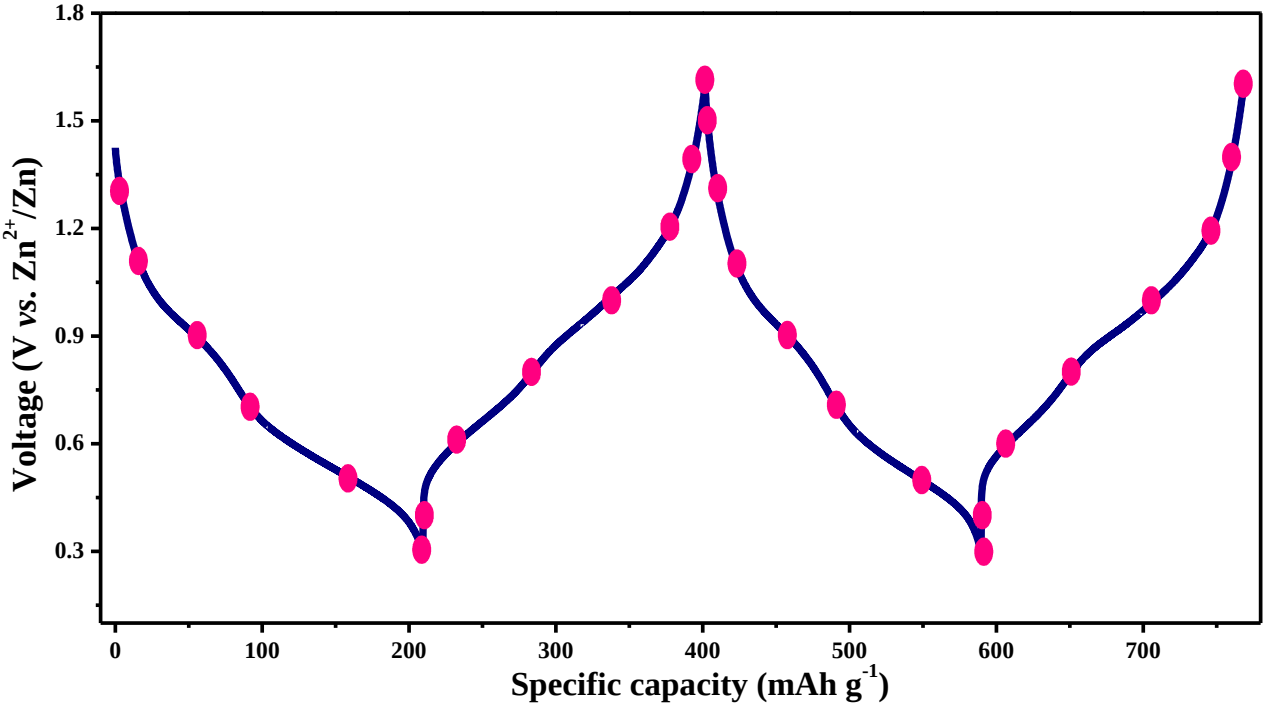

Figure S9. Charge/discharge profile in the first two cycles that are measured at a current density of 50 mA g^{-1}. The pink dots on the curves correspond to the selective electrode materials at different discharge/charge states with 0.1 V intervals, as shown below.

The first cycle (the open circuit voltage of $Zn/H_{11}Al_2V_6O_{23.2}$ battery is *ca.* 1.41 V):

Discharge to 1.3, 1.1, 0.9, 0.7, 0.5, and 0.3 V, respectively;

Charge to 0.4, 0.6, 0.8, 1.0, 1.2, 1.4, and 1.6 V, respectively.

The second cycle:

Discharge to 1.5, 1.3, 1.1, 0.9, 0.7, 0.5, and 0.3 V, respectively;

Charge to 0.4, 0.6, 0.8, 1.0, 1.2, 1.4, and 1.6 V, respectively.

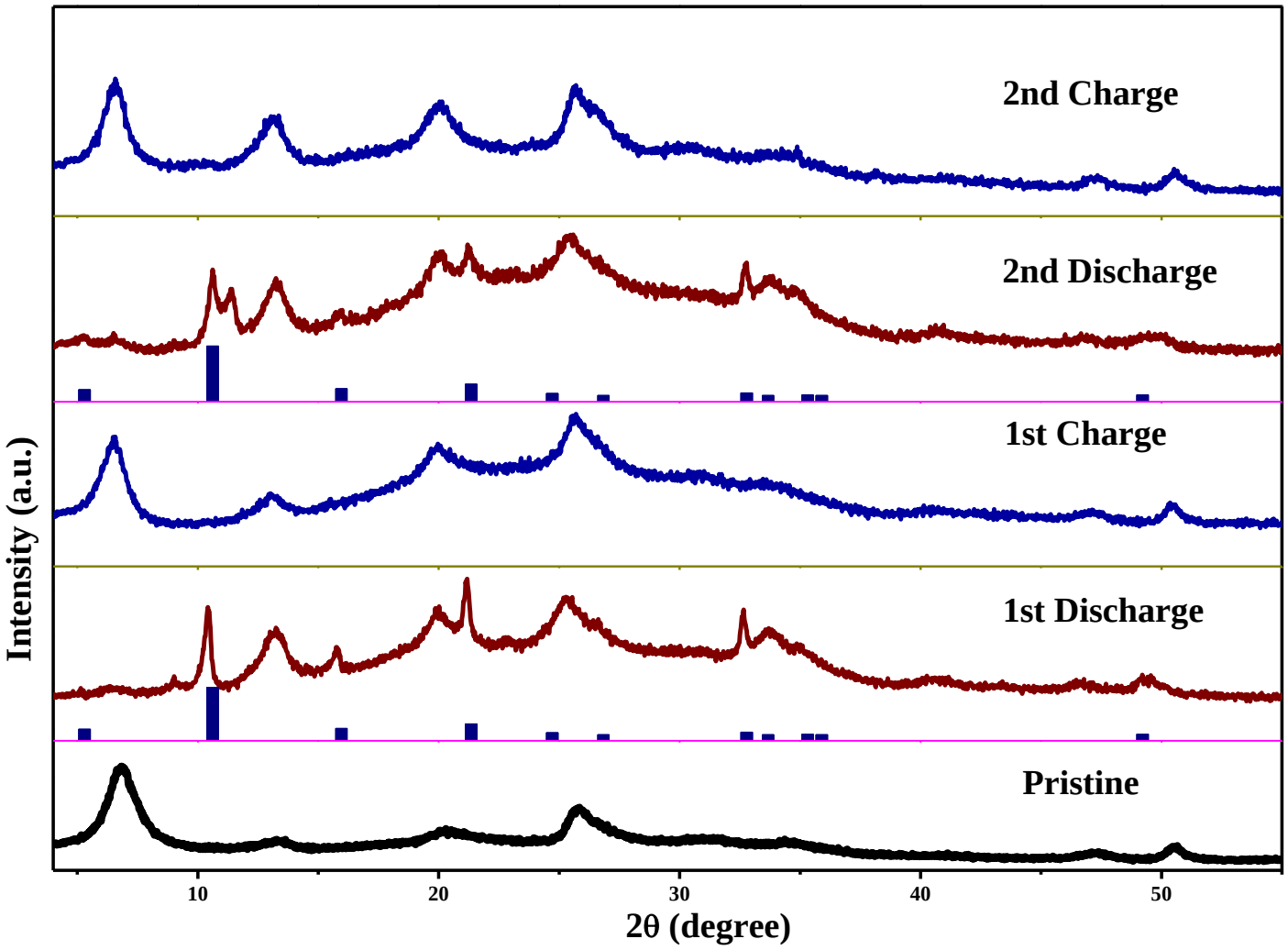

Figure S10. XRD patterns of the pristine, the fully discharged and charged electrodes in the first two cycles. A new material generates during the first discharged state, which can be indexed to basic zinc salt (BZS, $Zn_4ClO_4(OH)_7$), disappears in the subsequent charge process.

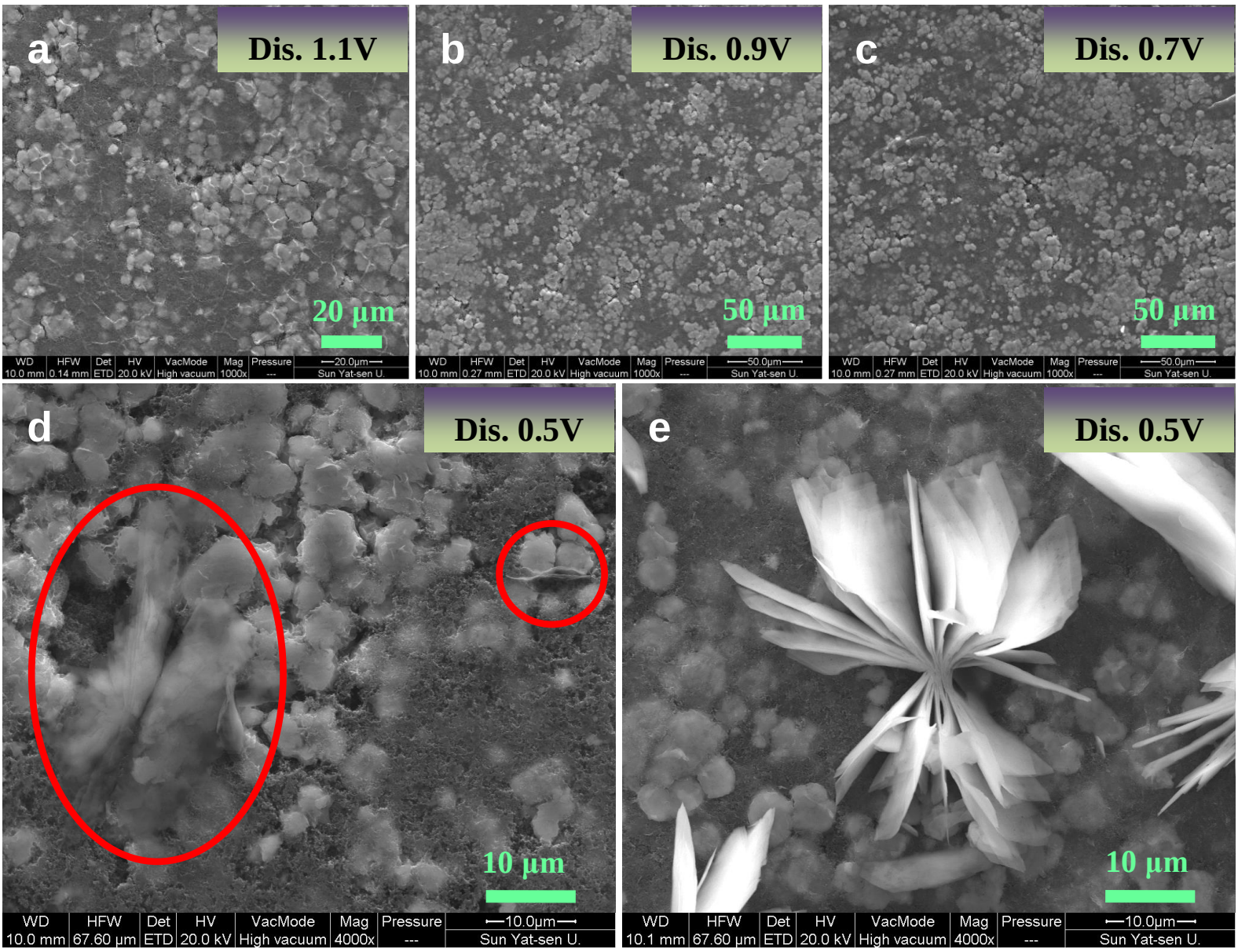

Figure S11. SEM images of the discharged electrodes obtained at different stages: a) 1.1 V, b) 0.9 V, c) 0.7 V, d) and e) 0.5 V. The BZS with layered structure is observed and detected when discharged to 0.5 V (Figure 2a), and interestingly is found generating from the surface of $H_{11}Al_2V_6O_{23.2}$, as exhibited in d) with red markers.

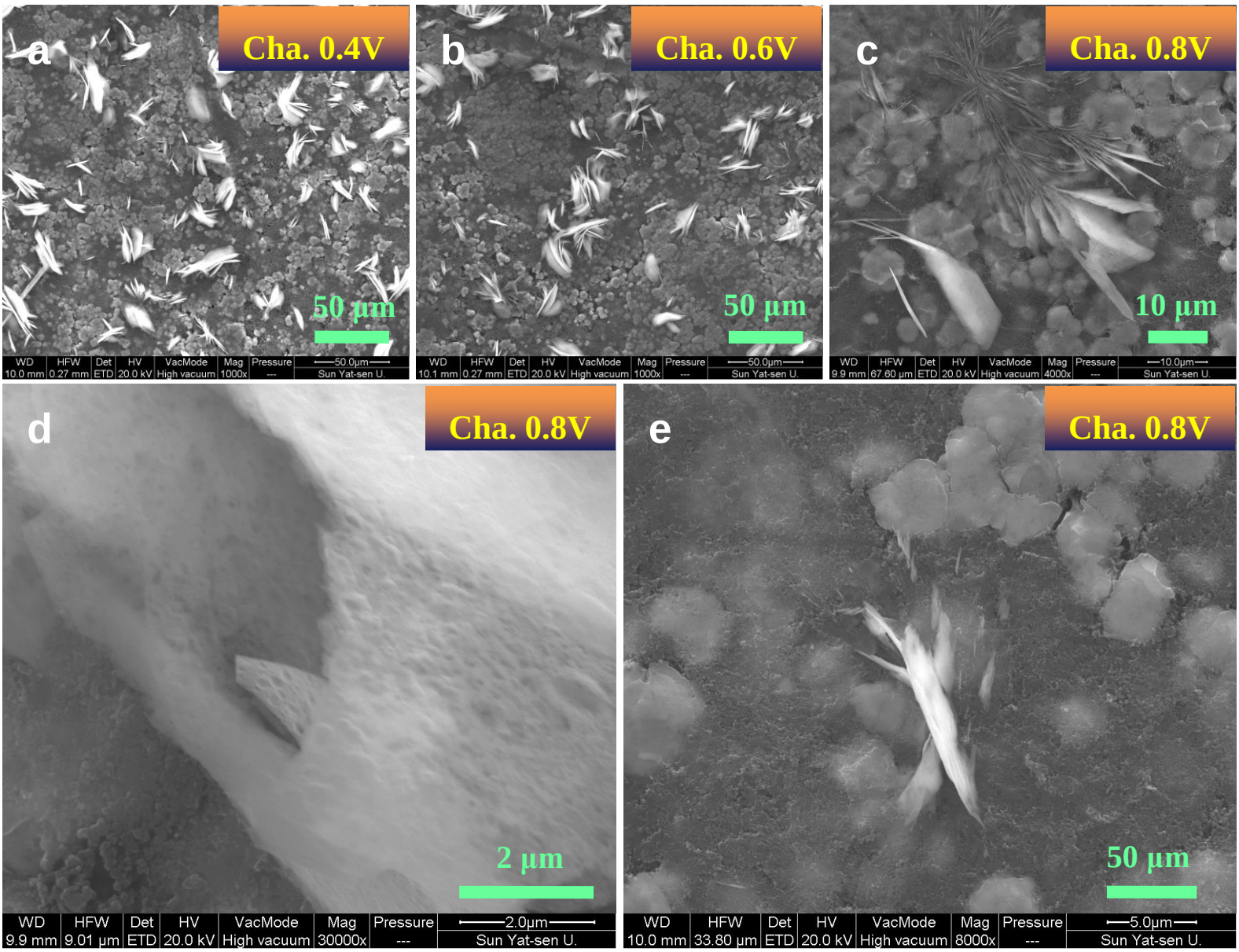

Figure S12. SEM images of the charged electrodes obtained at different stages: a) 0.4 V, b) 0.6 V, c), d), and e) 0.8 V. The content of BZS on the electrode surface gradually decreases upon charge process. The SEM image in c) depicts the disappearing BZS sheets. A magnified SEM image in d) suggests that the BZS sheet is assembled with small particles. Besides, the roots anchored on the surface of $H_{11}Al_2V_6O_{23.2}$ in e) further confirm our speculation of the growth process of BZS.

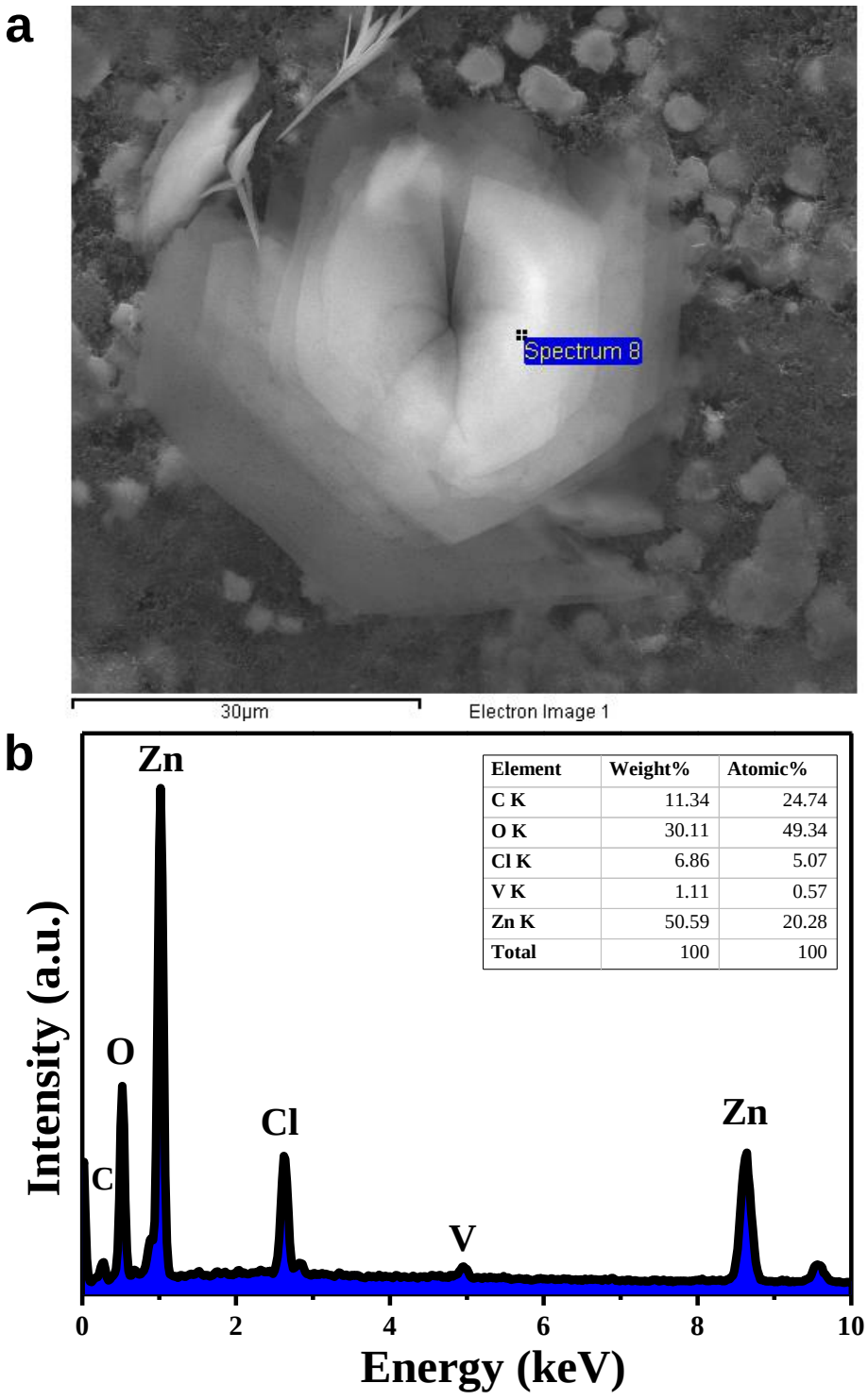

Figure S13. a) SEM image of the BZS sheets. b) EDX spectra obtained at the area marked in a). Inset in b) gives the measured elemental contents.

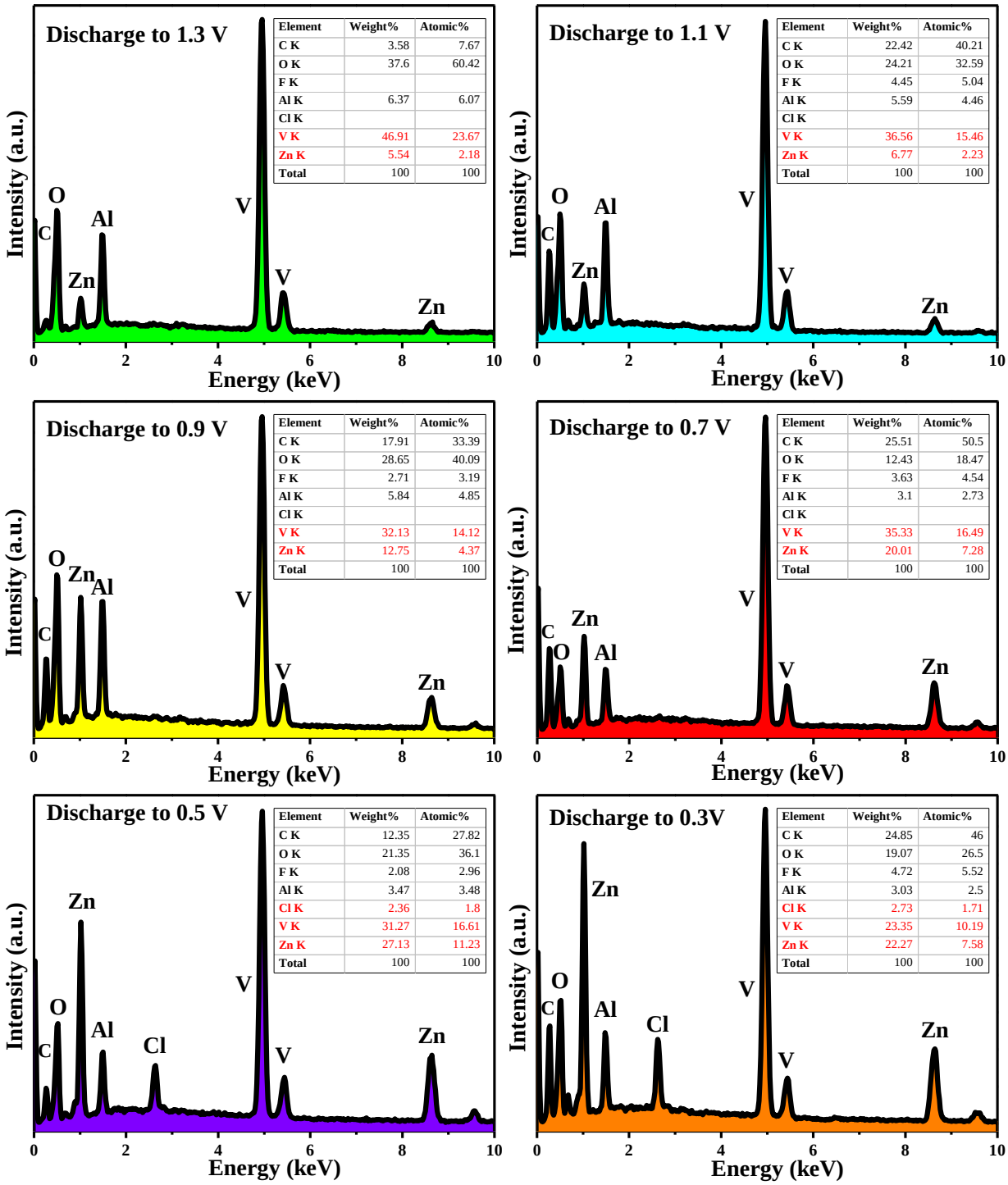

Figure S14. EDX spectra obtained at the different discharge processes. Noting that the EDX spectra are measured from point analyses by focusing the electron beams on the $H_{11}Al_2V_6O_{23.2}$ particles.

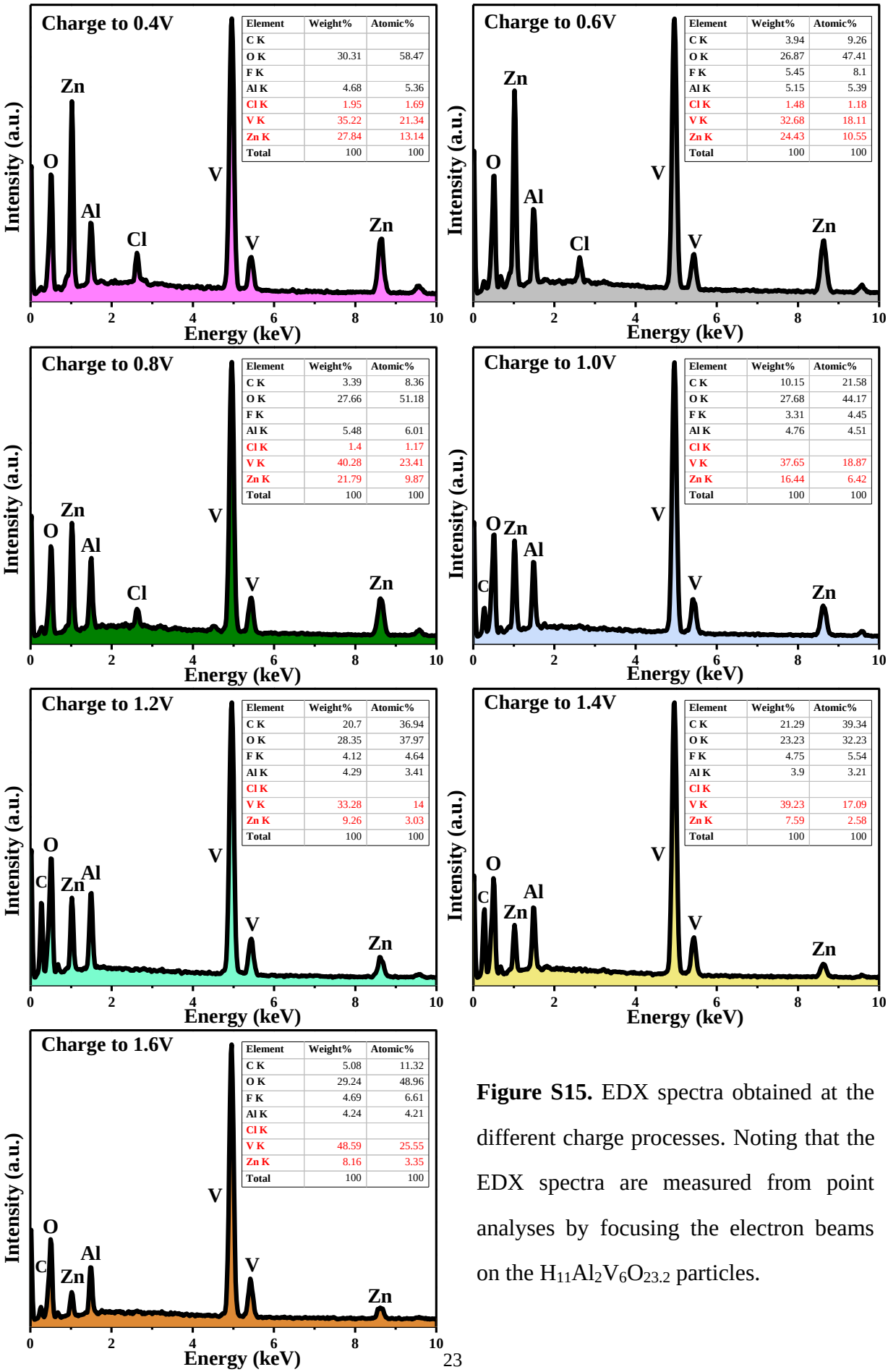

Figure S15. EDX spectra obtained at the different charge processes. Noting that the EDX spectra are measured from point analyses by focusing the electron beams on the $H_{11}Al_2V_6O_{23.2}$ particles.

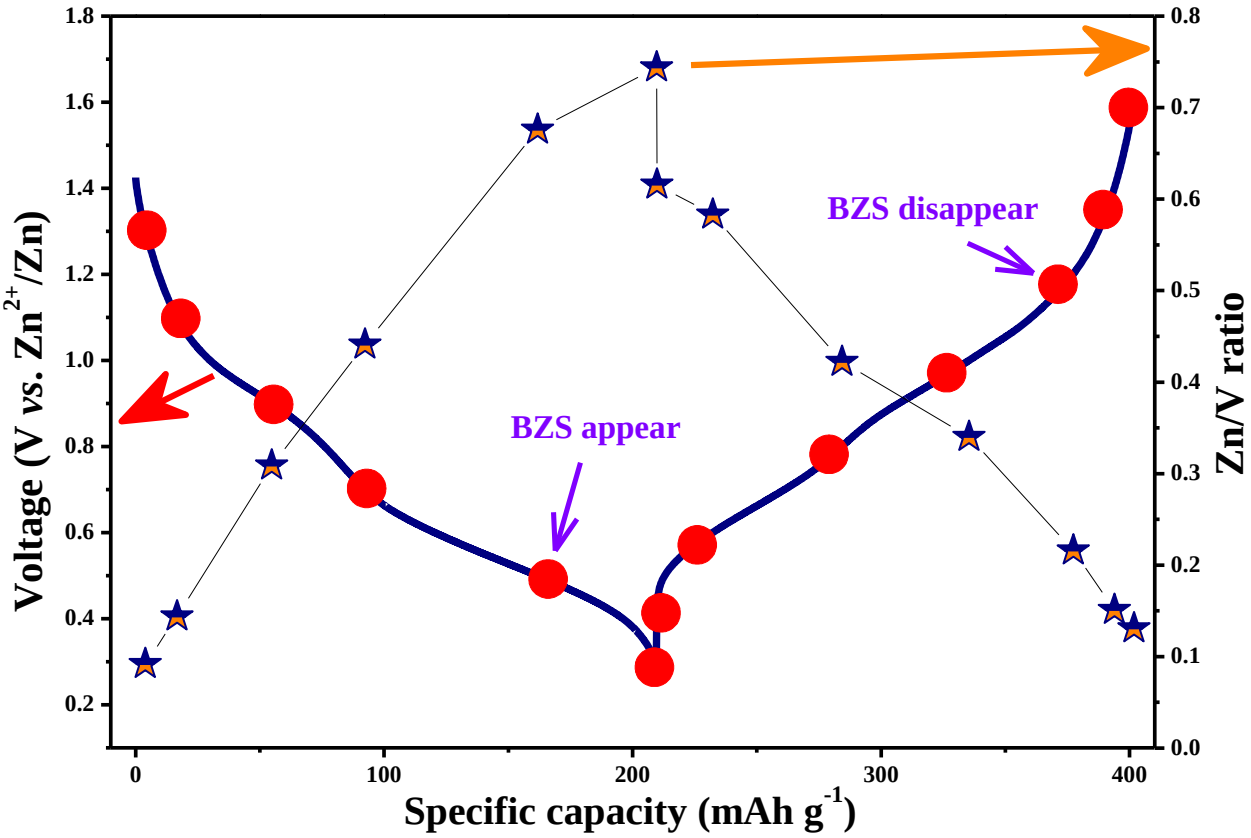

Figure S16. The content ratio of Zn and V at different discharge and charge stages in the first cycle. The Zn/V ratios show good agreement with Zn^{2+} insertion/extraction processes.

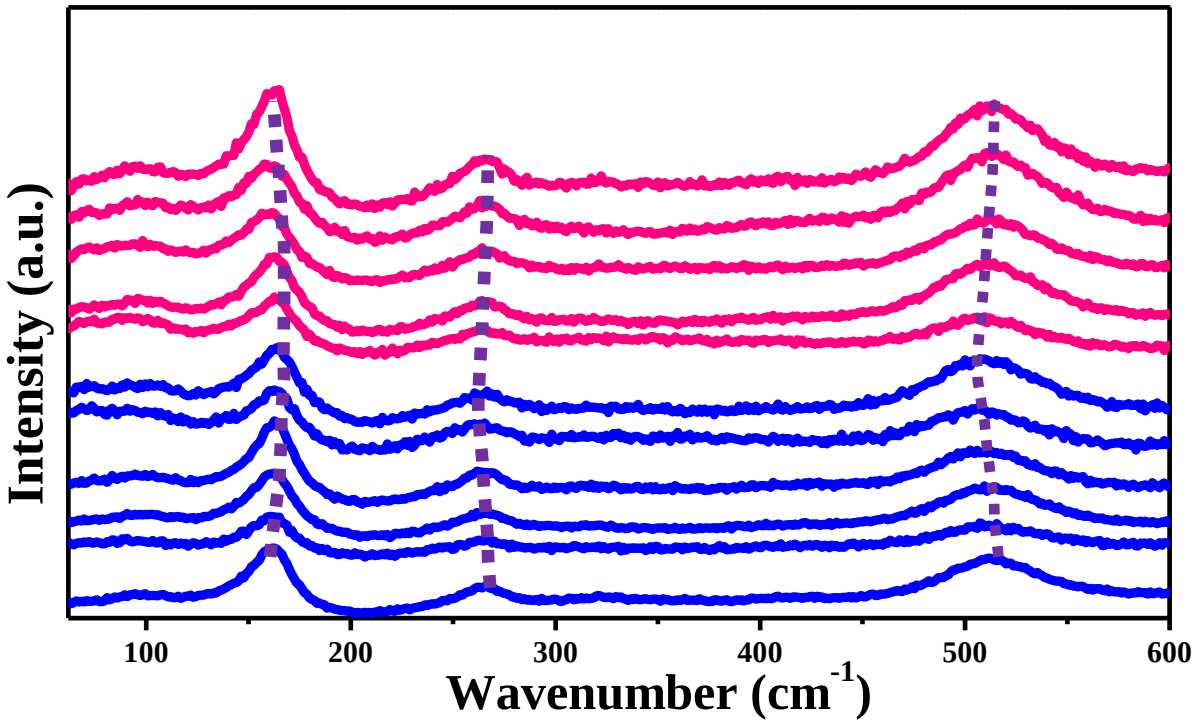

Figure S17. Raman spectra of the $H_{11}Al_2V_6O_{23.2}$ electrodes obtained in the second cycle at selected states. The blue and pink lines refer to the discharged and charged states. An opposite trend in the Raman shifts is detected for the peaks below and above 200 cm^{-1} under discharging and charging conditions, which is adverse to our previous studies about the zinc-storage properties in $NH_4V_4O_{10}$. It is known that the stress state and the surrounding environmental changes can be studied according to the Raman spectra of the materials. Therefore, there must be differential interaction of Zn^{2+} with the vanadium oxides skeletons.

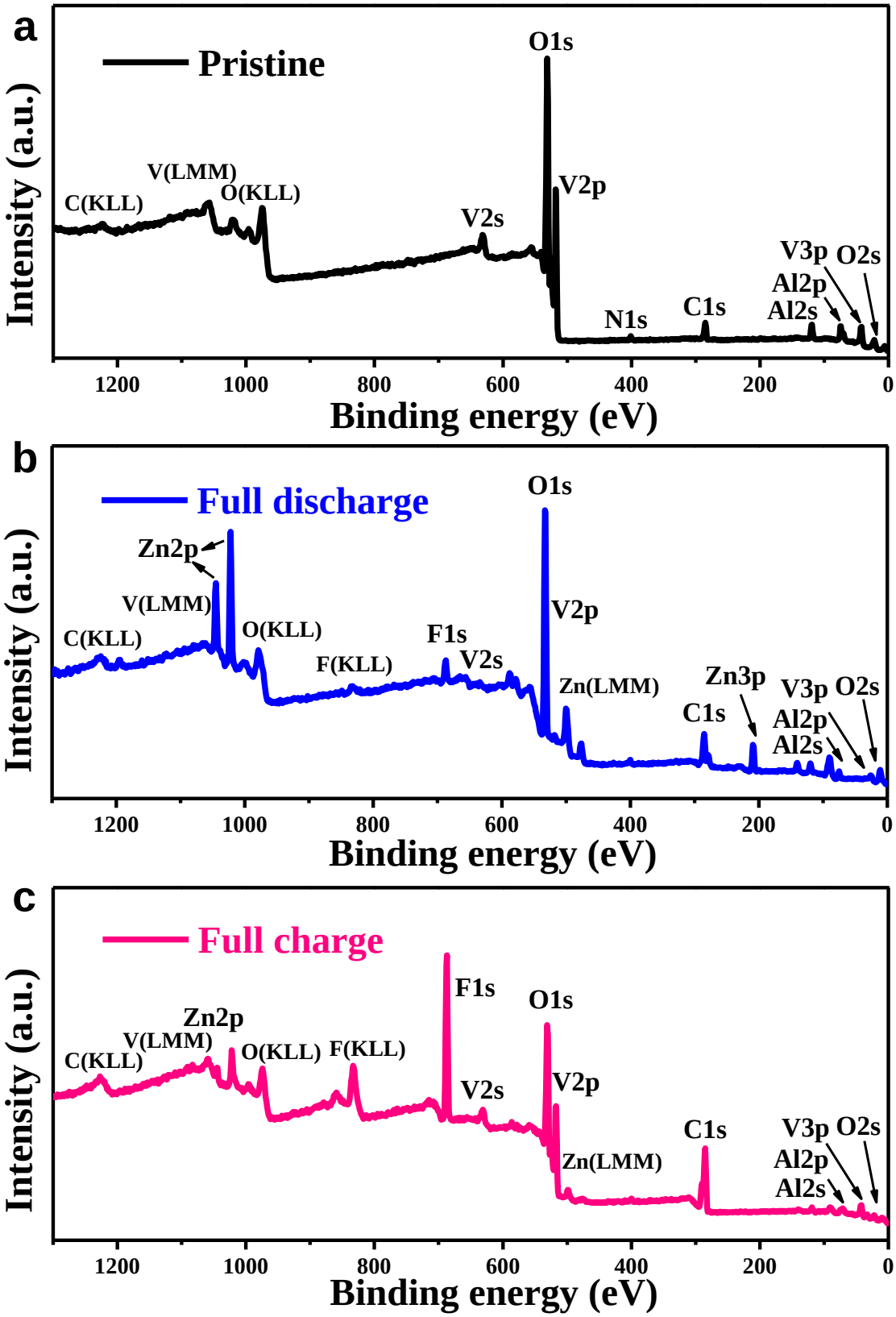

Figure S18. XPS characterizations of the $H_{11}Al_2V_6O_{23.2}$ electrode materials. Survey spectra obtained at a) Pristine, b) fully discharged state, and c) fully charged state.

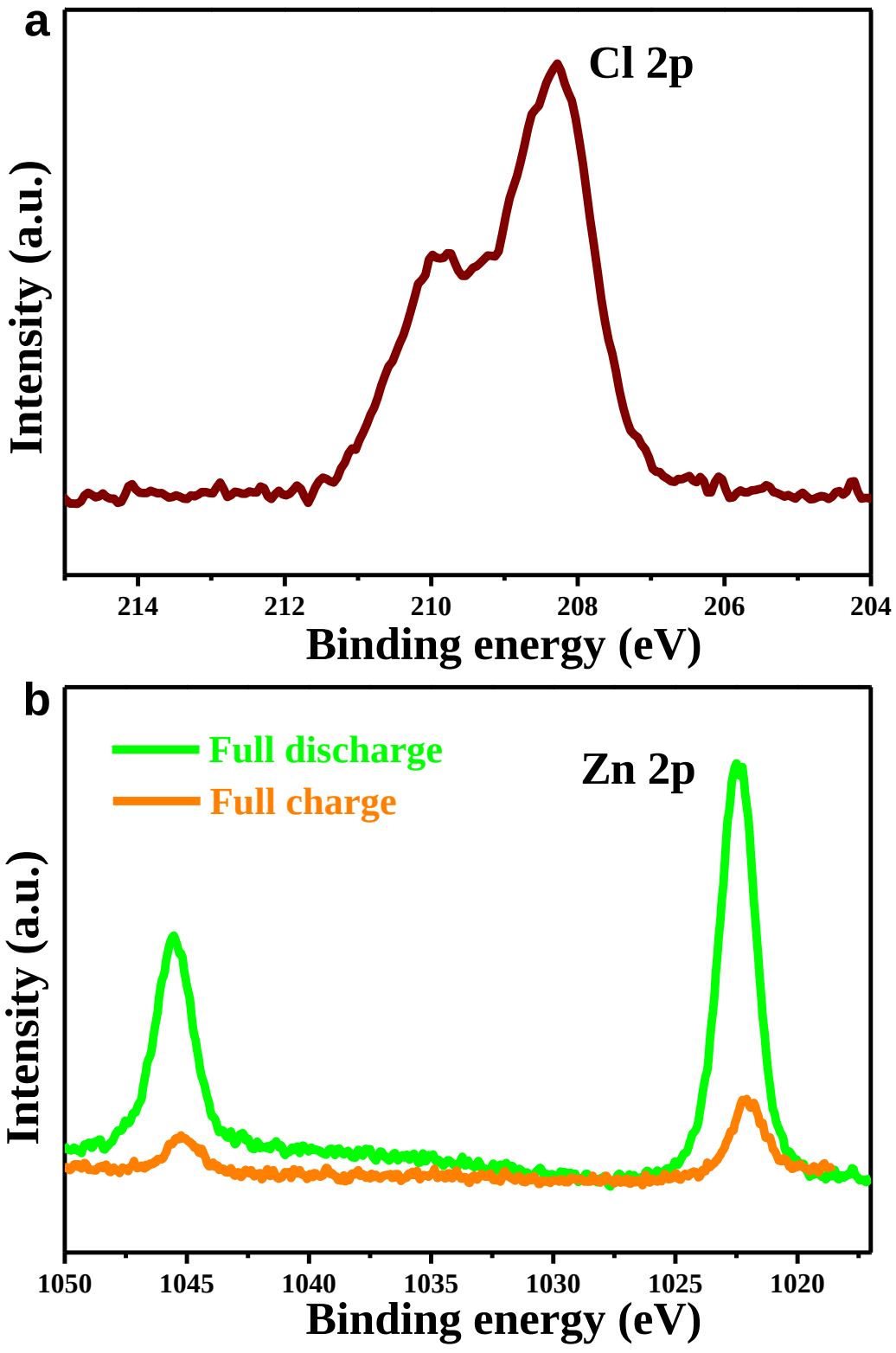

Figure S19. XPS characterizations of the $H_{11}Al_2V_6O_{23.2}$ electrode materials. a) Cl 1*s* region detected at fully discharged state. b) Zn 2*p* region obtained at fully discharged and charged state.

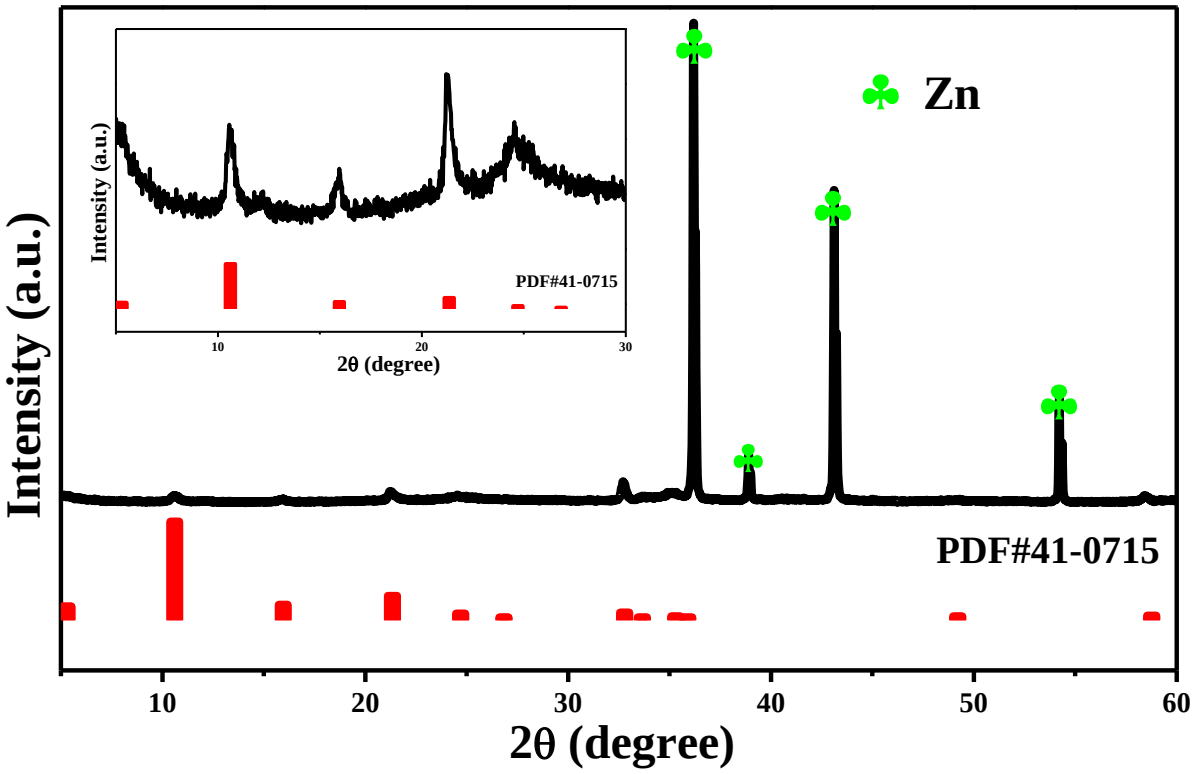

Figure S20. XRD patterns of the Zn anode obtained at the fully charged state in the first cycle. Inset shows the magnified region between 5 – 30 °, in which one can see that the XRD patterns can be well indexed to monoclinic $Zn_4(OH)_7ClO_4$ (JCPDS no. 41-0715).

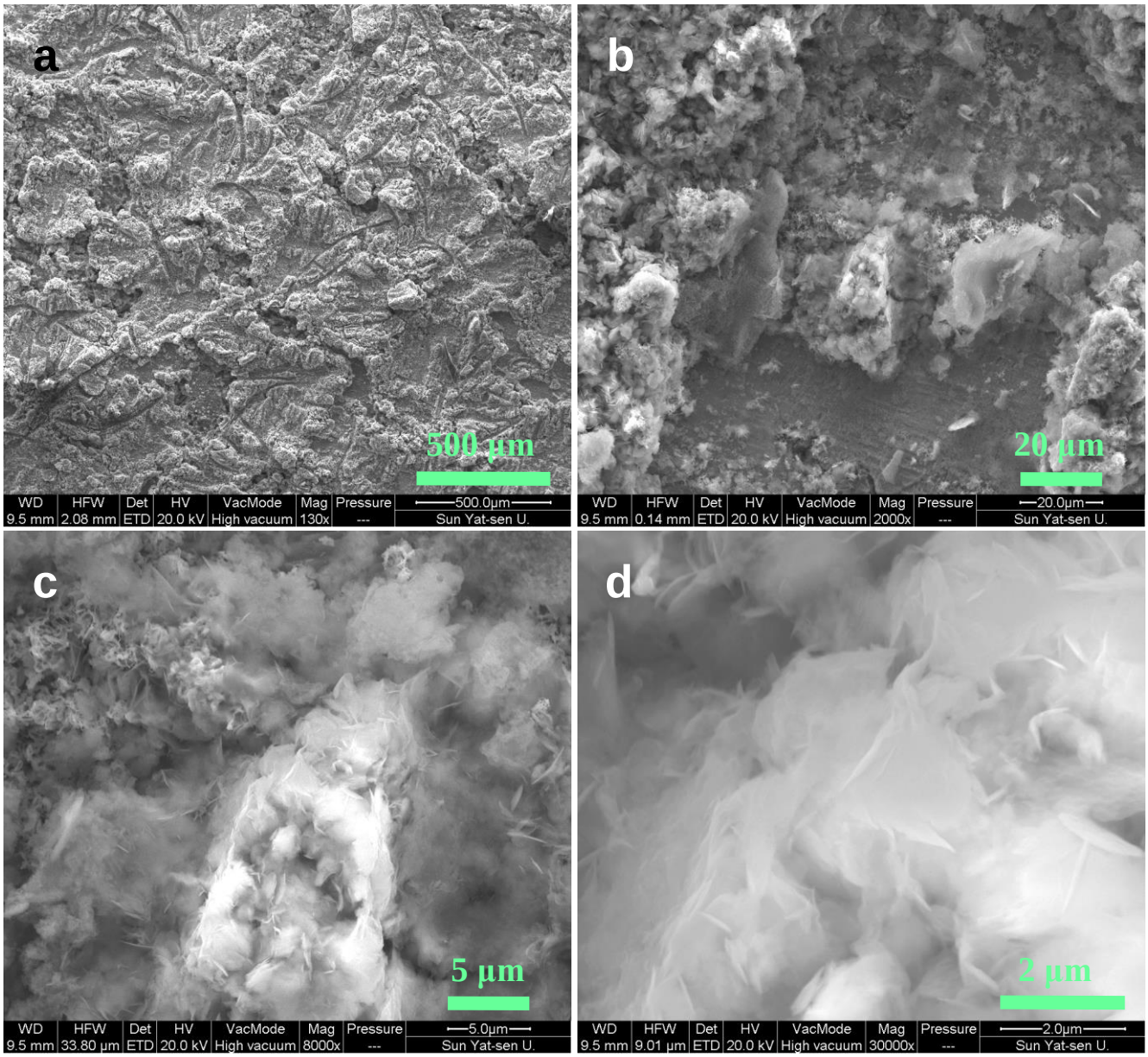

Figure S21. a – d) SEM images of the Zn anode obtained at the fully charged state in the first cycle. Upon charge process, the nonuniform deposition of zinc leads to the rough electrode surface. Considerable amount of sheet-like structure is observed on the surface of large particles.

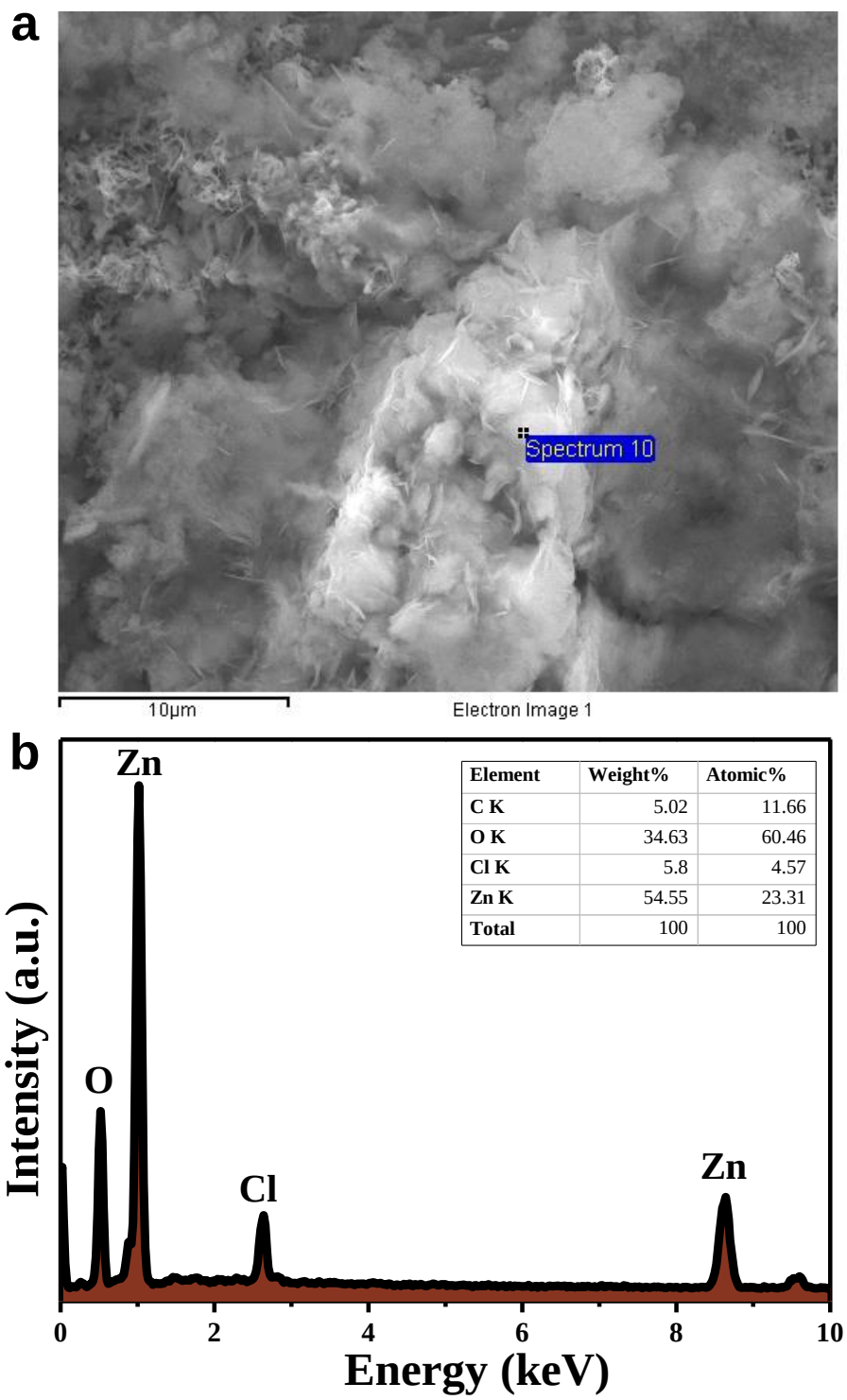

Element	Weight%	Atomic%
C K	5.02	11.66
O K	34.63	60.46
Cl K	5.8	4.57
Zn K	54.55	23.31
Total	100	100

Figure S22. a) SEM image of the Zn anode obtained at the fully charged state in the first cycle. b) EDX spectra obtained at the area marked in a). Inset in b) gives the measured elemental contents, while the EDS results match well with the XRD characterizations in Figure S20.

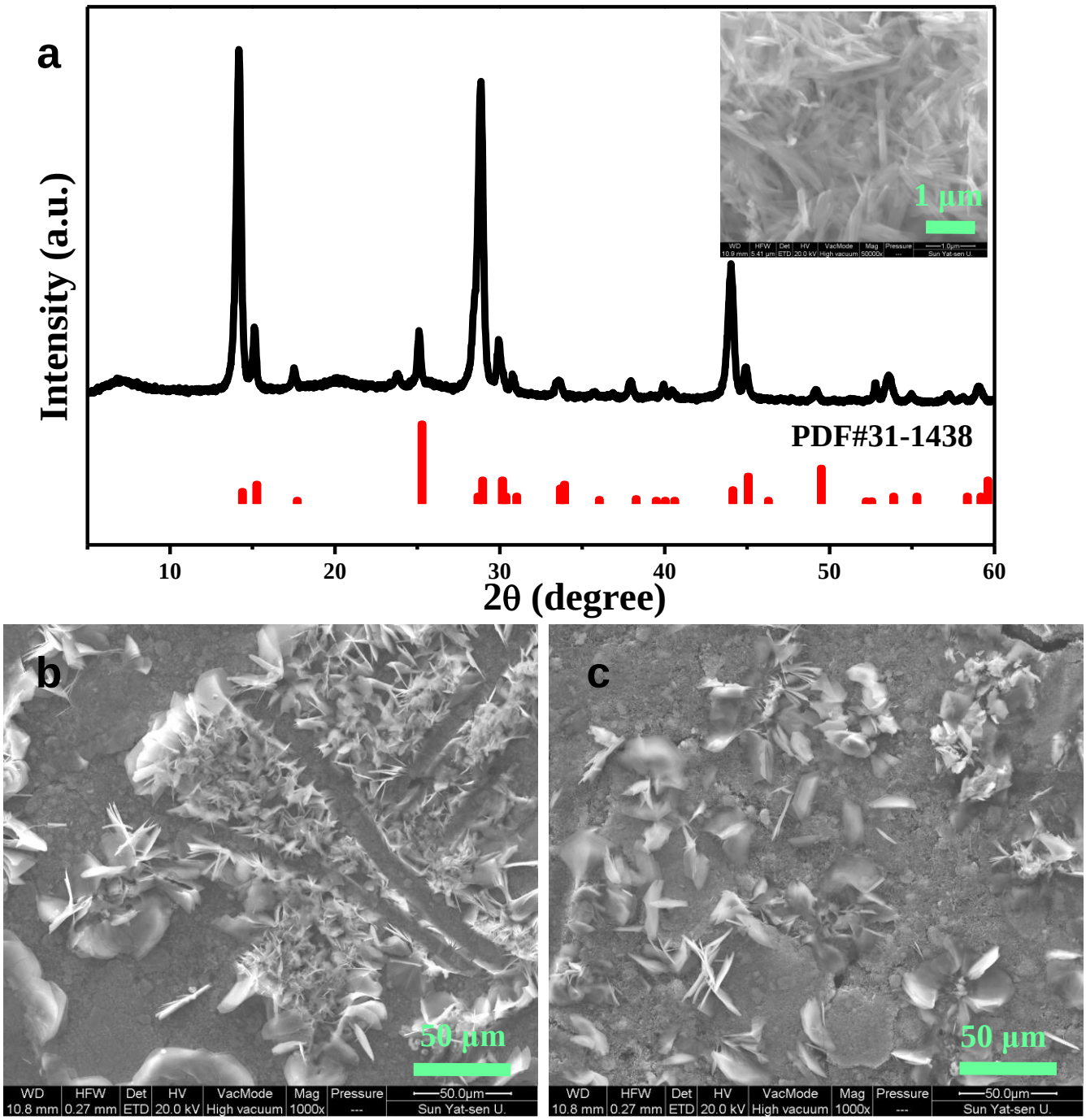

Figure S23. a) XRD patterns of the VO_2. Inset in a) shows the SEM image of VO_2. SEM images of b) fully discharged and c) fully charged VO_2 electrodes in the first cycle.

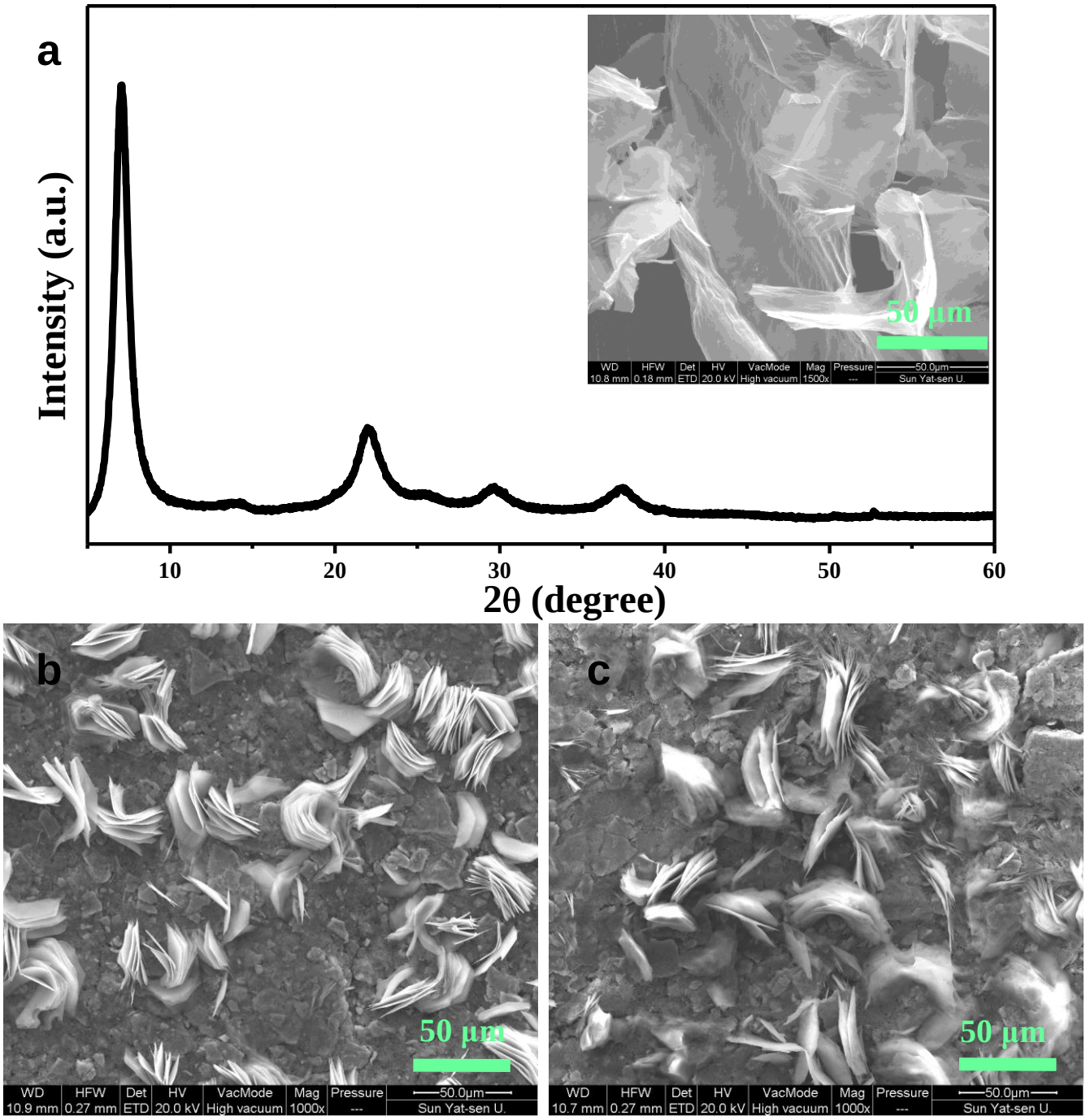

Figure S24. a) XRD patterns of the $V_5O_{12}\cdot 6H_2O$. Inset in a) shows the SEM image of $V_5O_{12}\cdot 6H_2O$. SEM images of b) fully discharged and c) fully charged $V_5O_{12}\cdot 6H_2O$ electrodes in the first cycle.

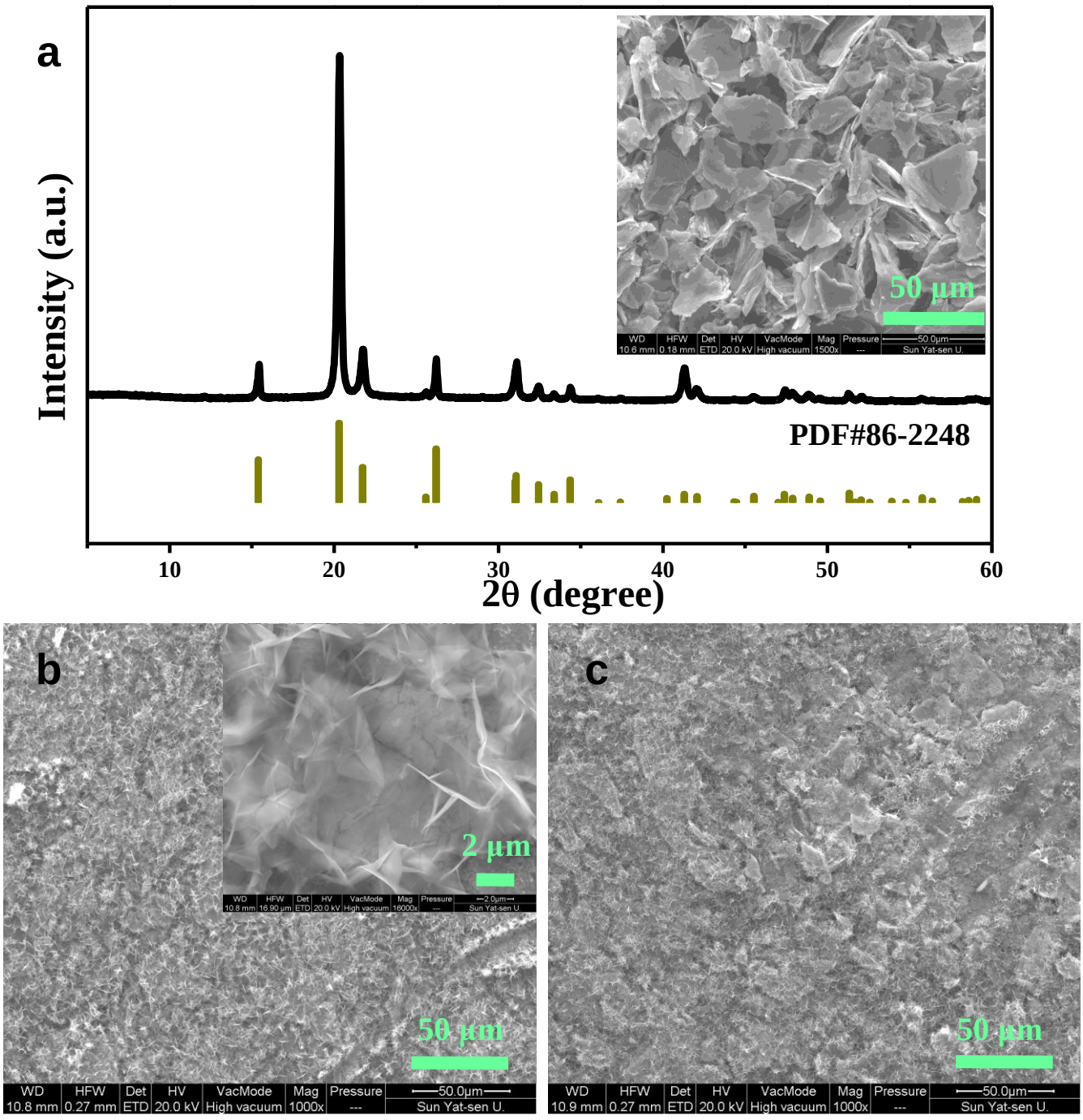

Figure S25. a) XRD patterns of the V_2O_5. SEM images of b) fully discharged and c) fully charged V_2O_5 electrodes in the first cycle. Insets in a) and b) show the SEM image of V_2O_5 and fully discharged V_2O_5 electrodes, respectively.

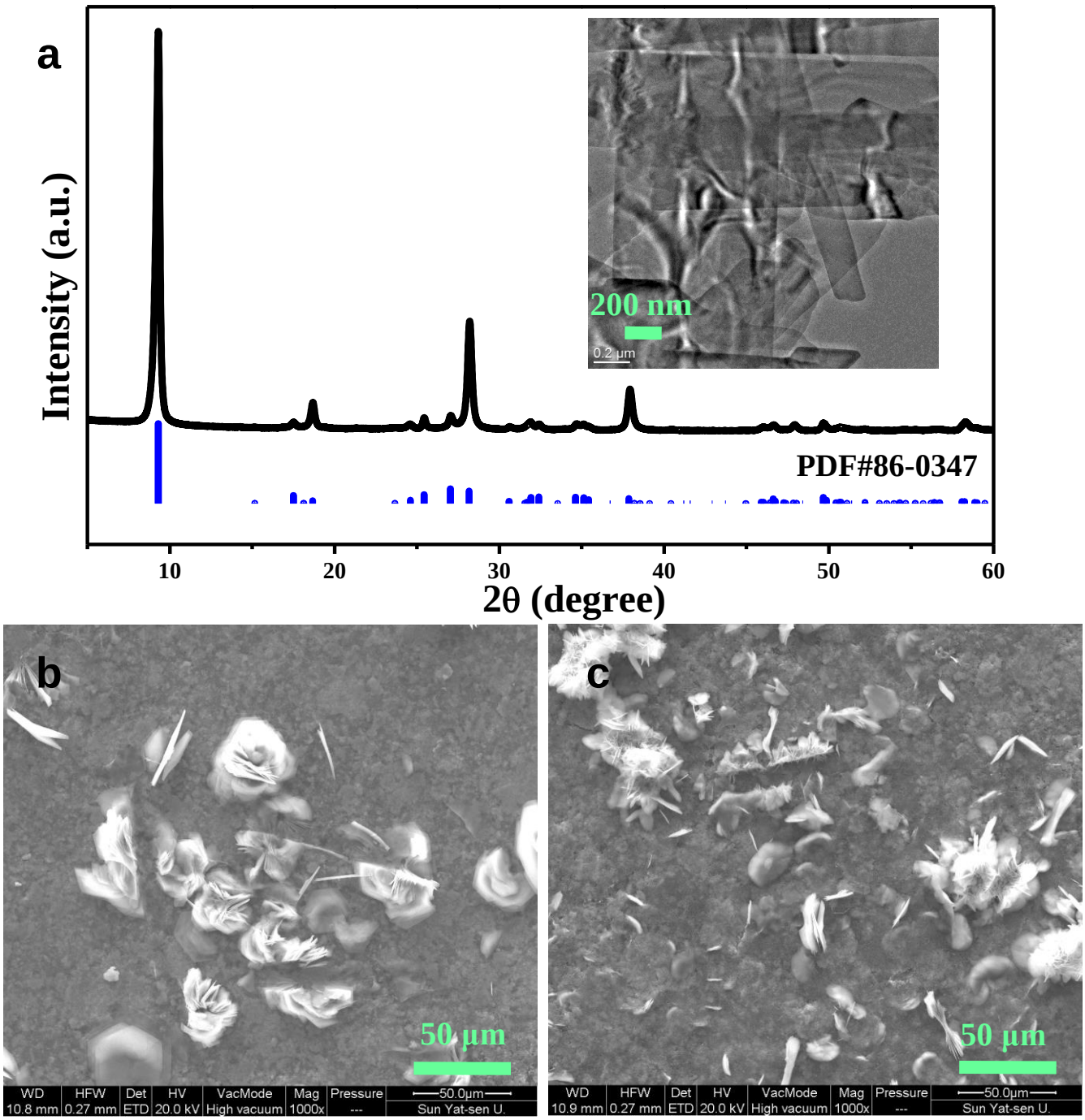

Figure S26. a) XRD patterns of the $K_{0.486}V_2O_5$. SEM images of b) fully discharged and c) fully charged $K_{0.486}V_2O_5$ electrodes in the first cycle. Inset in a) shows the TEM image of $K_{0.486}V_2O_5$.

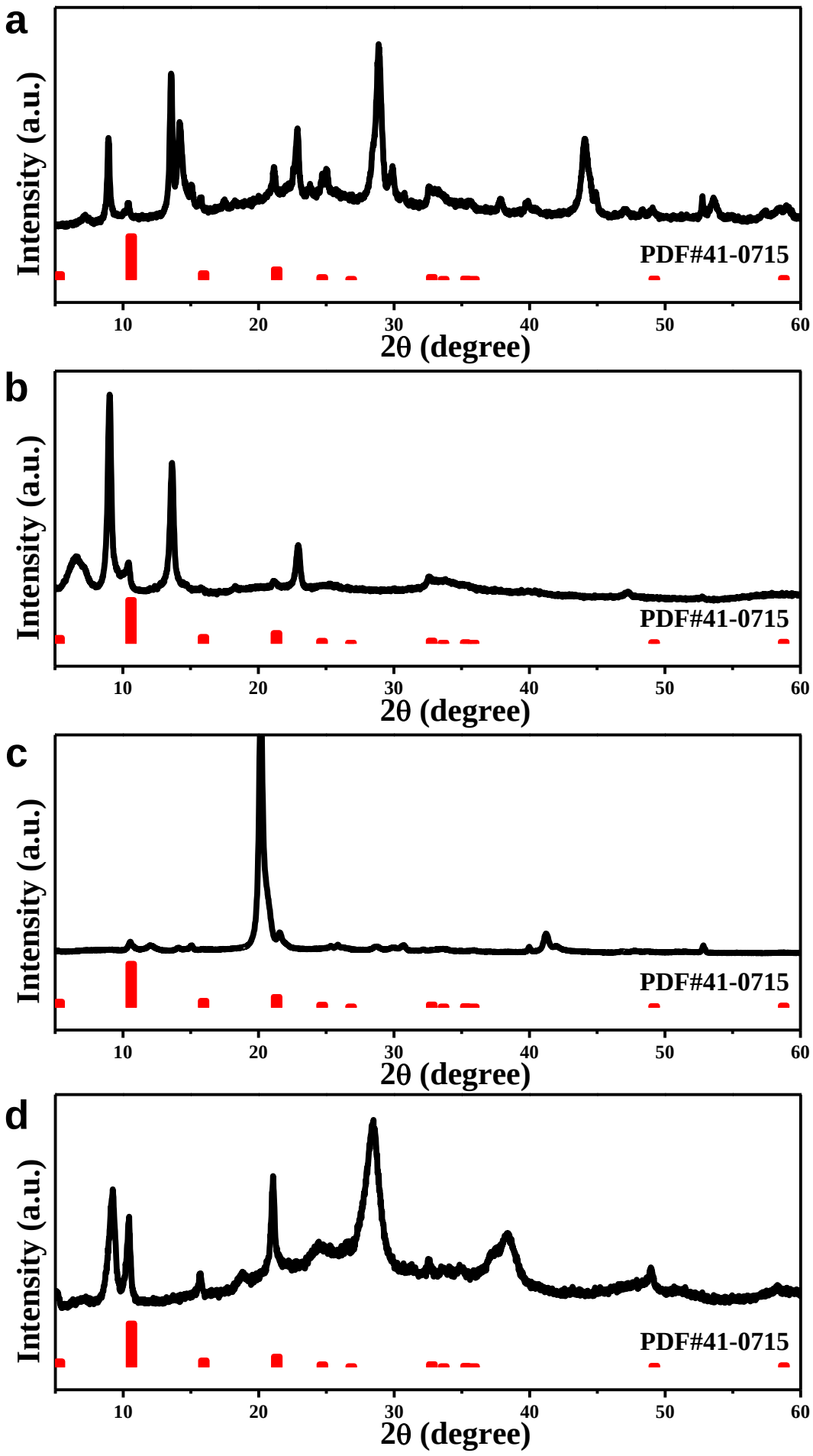

Figure S27. XRD patterns of the fully discharged electrodes: a) VO_2, b) $V_5O_{12}\cdot 6H_2O$, c) V_2O_5, and d) $K_{0.486}V_2O_5$, respectively.

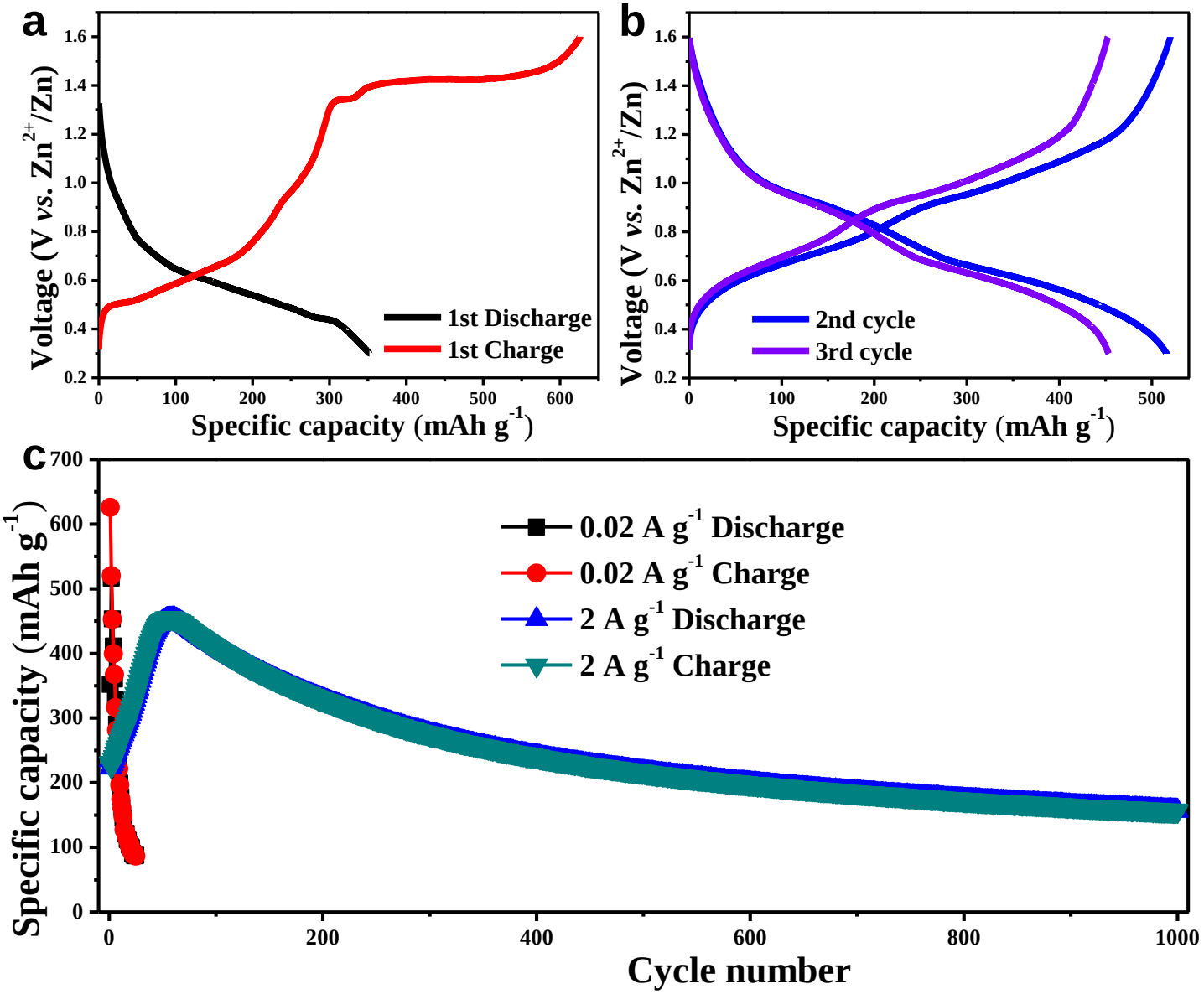

Figure S28. a, b) Charge-discharge profiles in the initial three cycles. c) Cycling performance of the VO_2 electrodes at different current densities.

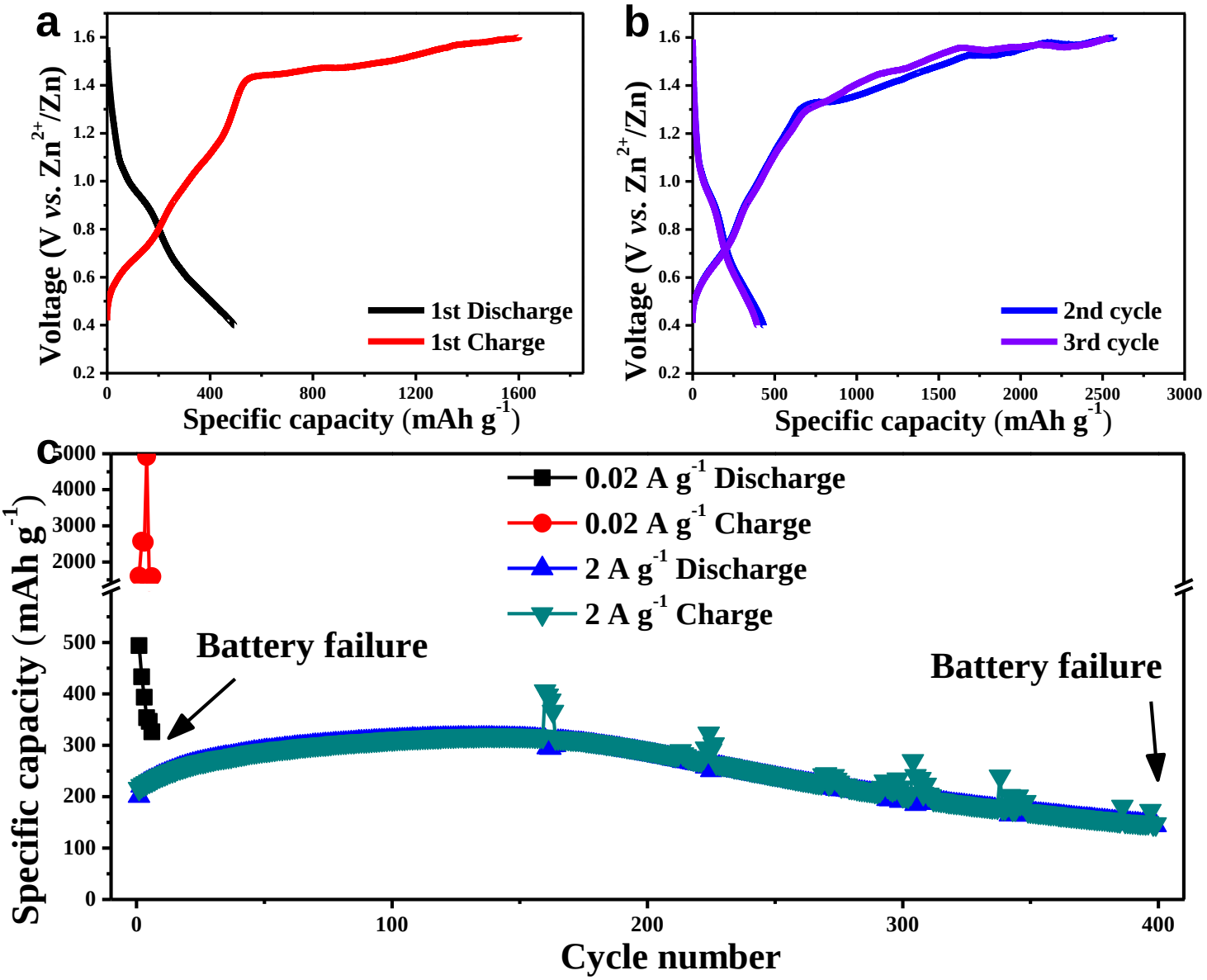

Figure S29. a, b) Charge-discharge profiles in the initial three cycles. c) Cycling performance of the $V_5O_{12}·6H_2O$ electrodes at different current densities. The charge capacity is far higher than the discharge capacity at 0.02 A g^{-1}, while the charge capacity gradually increases with prolonging cycles. We think that the massive accumulation of irreversible BZS leads to difficult extraction of Zn^{2+}, which resulting to this abnormal phenomenon.

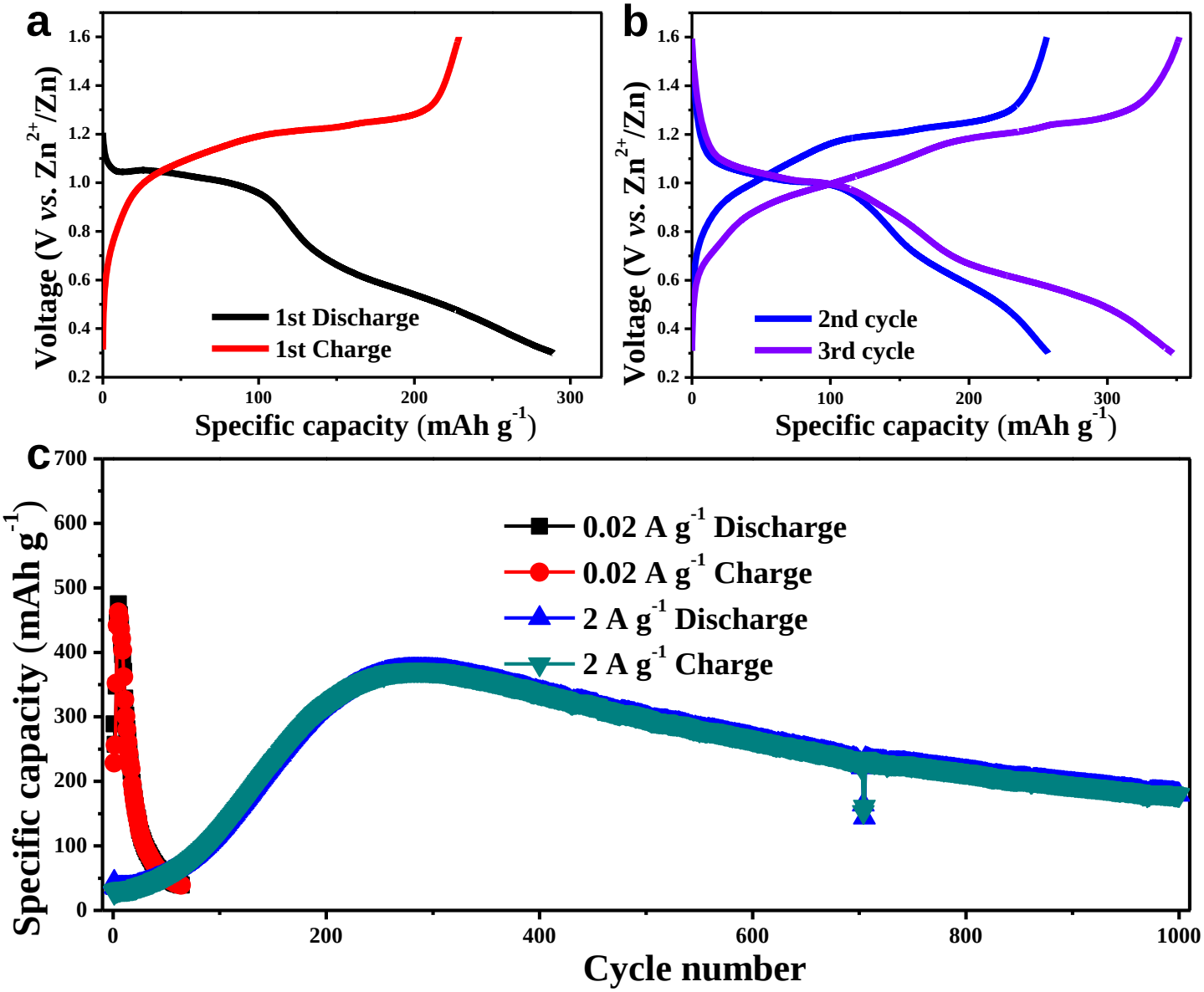

Figure S30. a, b) Charge-discharge profiles in the initial three cycles. c) Cycling performance of the V_2O_5 electrodes at different current densities.

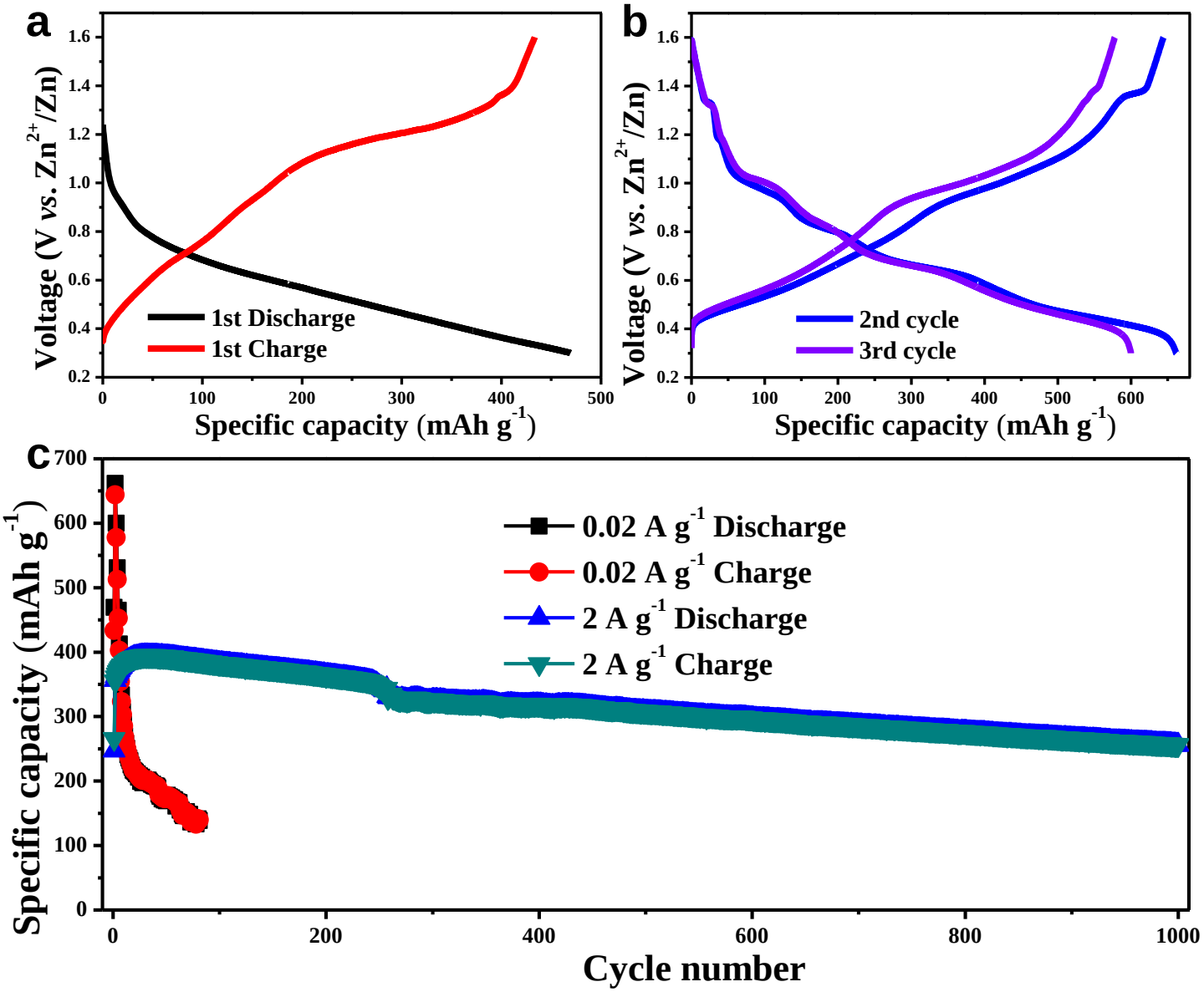

Figure S31. a, b) Charge-discharge profiles in the initial three cycles. c) Cycling performance of the $K_{0.486}V_2O_5$ electrodes at different current densities.

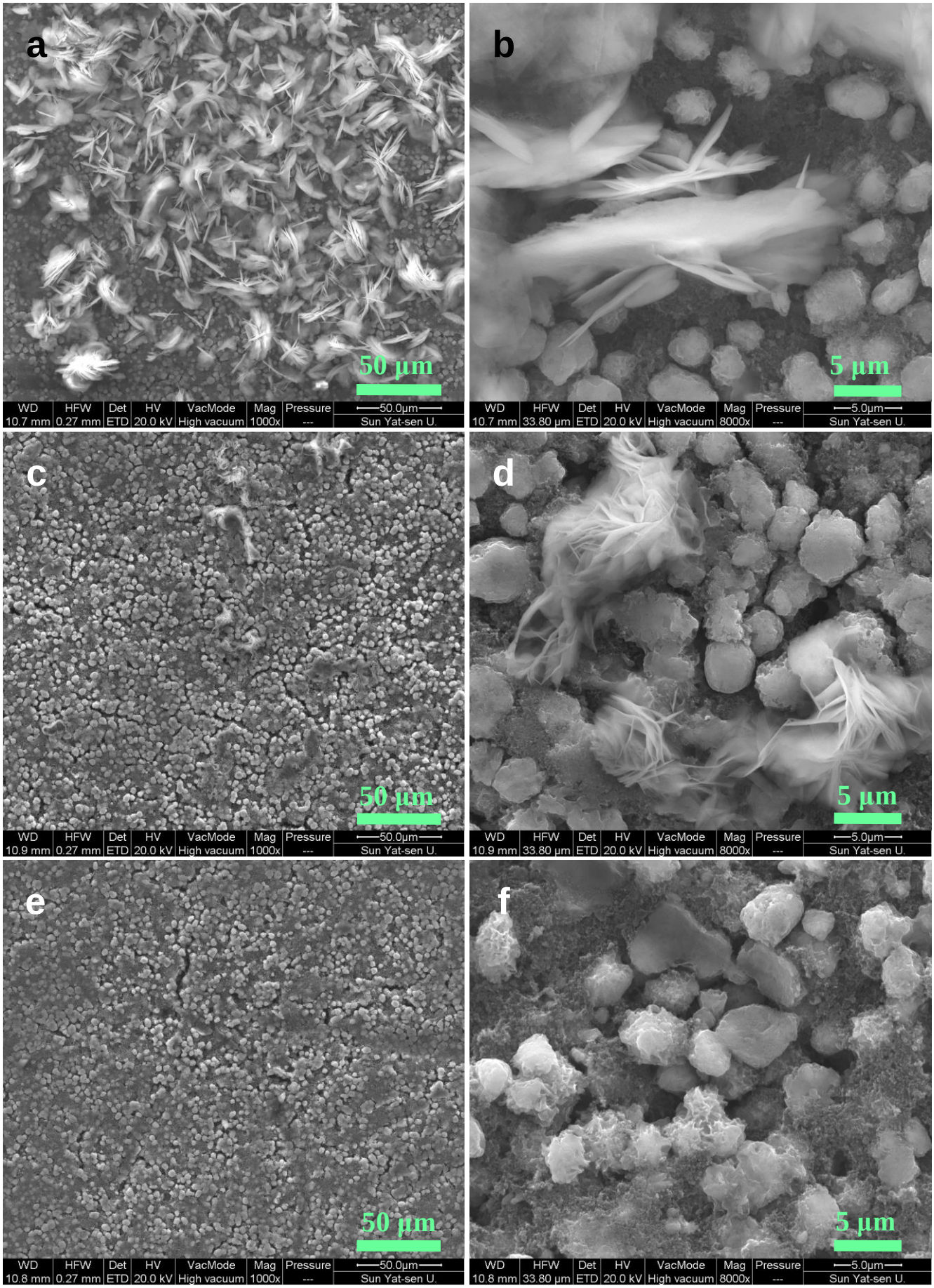

Figure S32. SEM images of the fully charged $H_{11}Al_2V_6O_{23.2}$ electrodes obtained after charge/discharge for three days at different current densities: a, b) 0.02 A g^{-1}, c, d) 0.2 A g^{-1}, and e, f) 2 A g^{-1}.

Figure S32 shows the SEM images of the $H_{11}Al_2V_6O_{23.2}$ electrodes obtained at fully charged states. In Figure S33a, the dense BZS sheets are observed on the electrode surface and much more than those in the first charge process (Figure 4a). After charge/discharge over three days, small account of BZS is firstly detected on the electrode surface when cycled at the current density of 0.2 A g^{-1}, as depicted in Figure S33c and d. By comparison, the BZS is still not found at the high current density. These results manifest the different amounts of BZS and reversibility for generation/disappearance at the different current densities. The gradual accumulation of irreversible BZS on the electrode surface will inevitably impede the further Zn^{2+} intercalation, leading to the capacity fading with prolonging cycles. In addition, through careful observation, the shape and size of $H_{11}Al_2V_6O_{23.2}$ spheres demonstrate the bigger changes in the high current compared with those in low current, as illustrated in Figure S32b, d, and f.

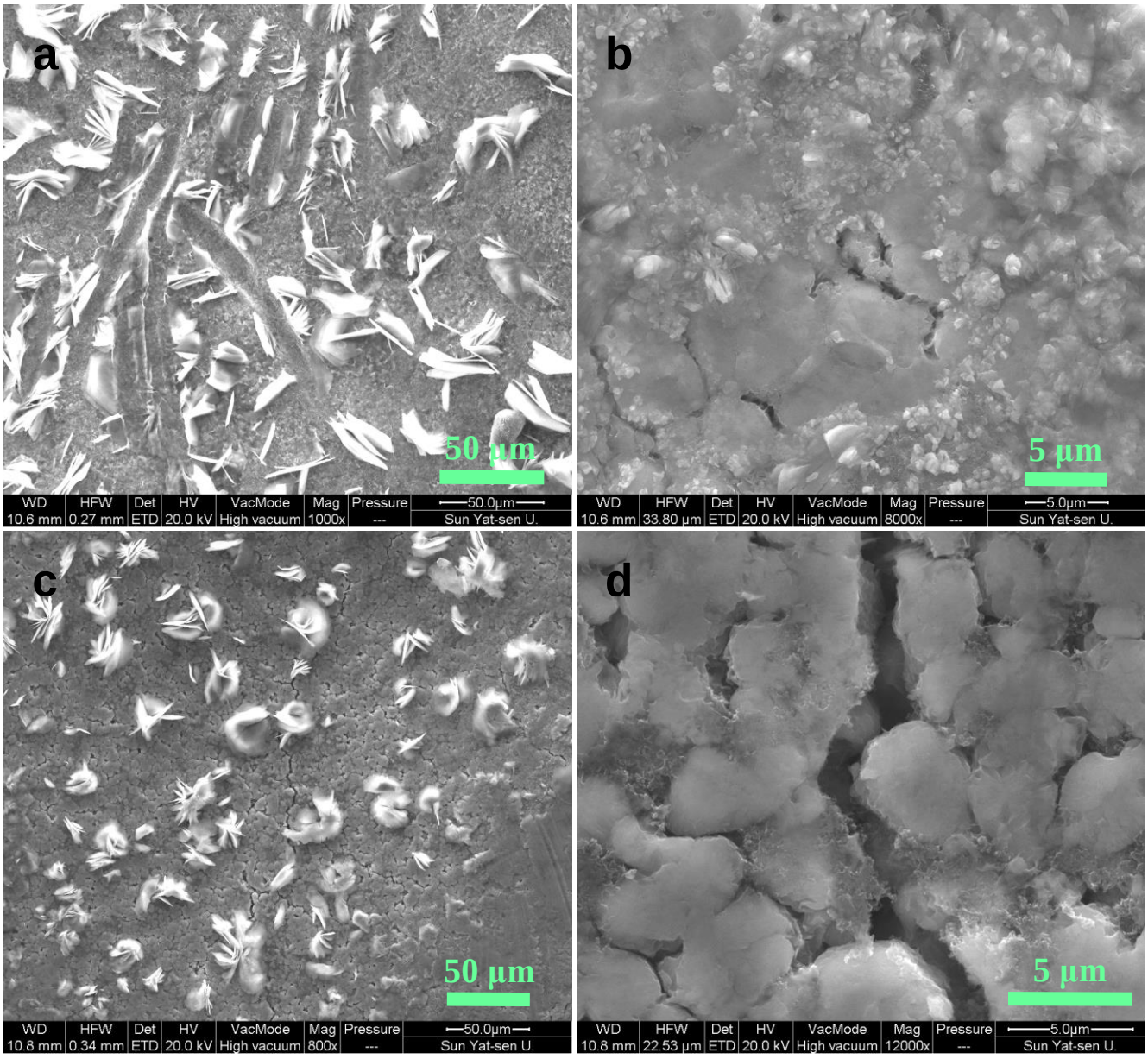

Figure S33. SEM images of the $H_{11}Al_2V_6O_{23.2}$ electrode obtained at the fully discharged state: a, b) top side and c, d) bottom side.

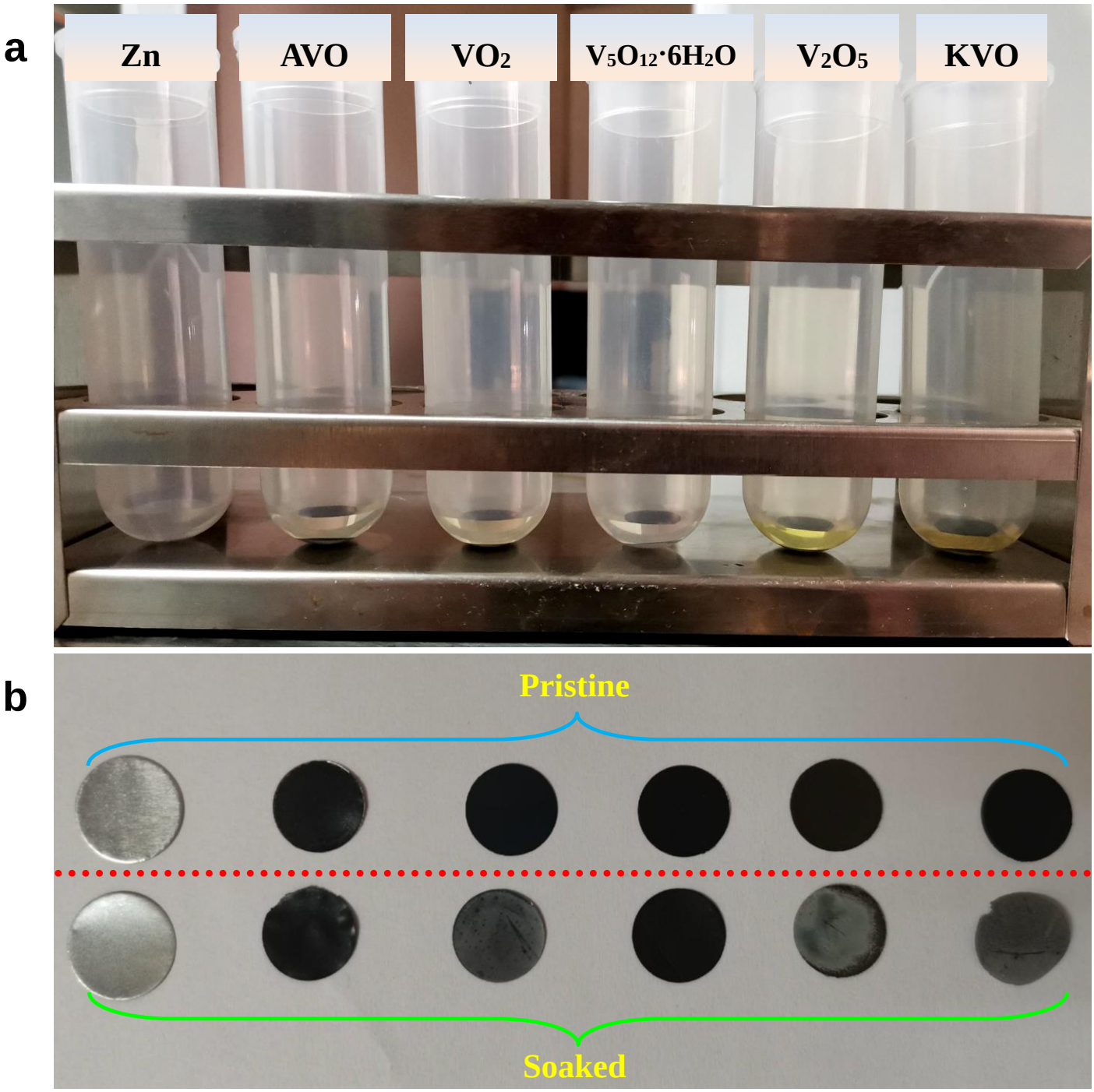

Figure S34. a) Optical image of the electrodes obtained after soaking in electrolyte for one day. b) Optical image of the fresh and soaked electrodes.

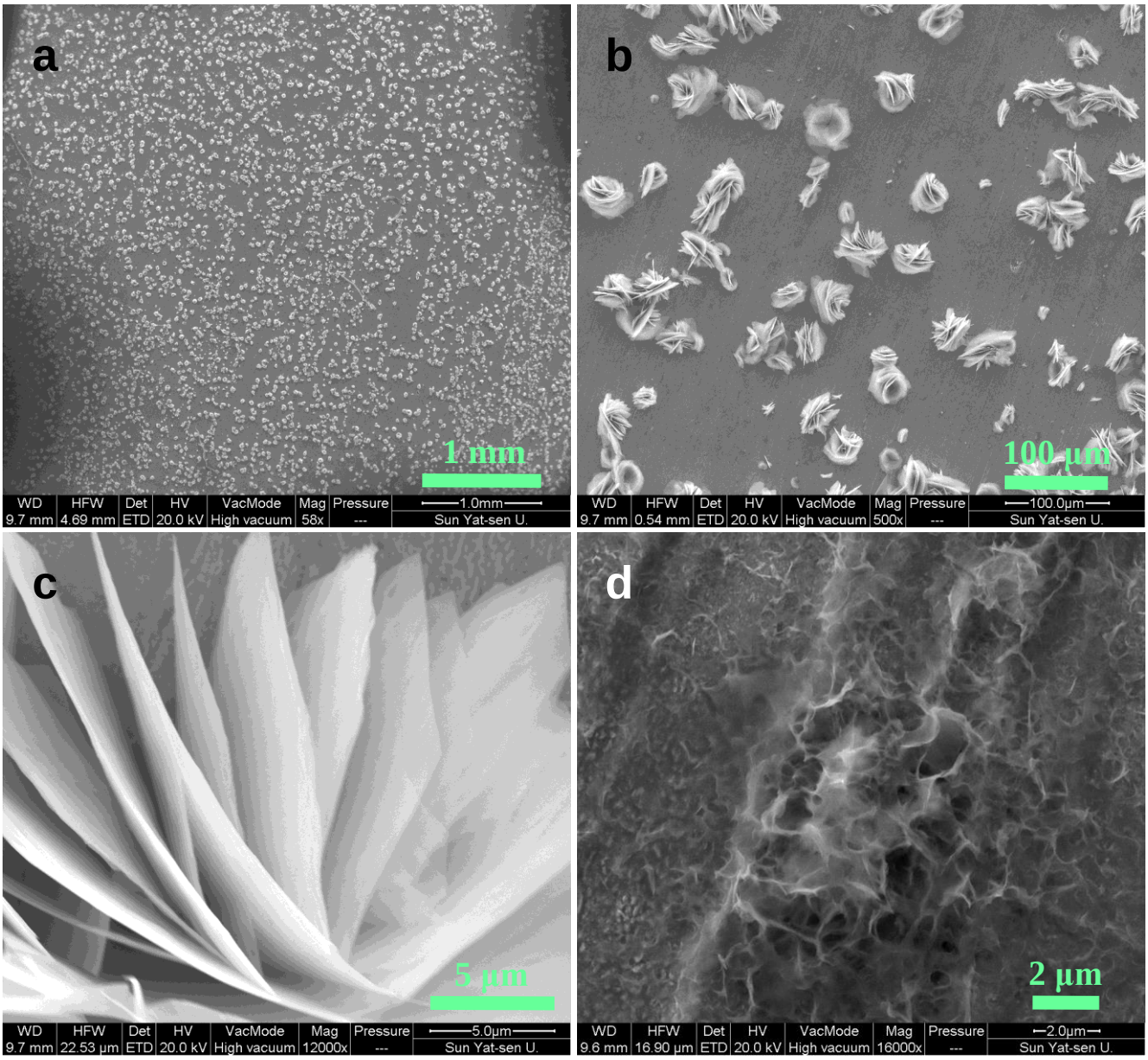

Figure S35. a – d) SEM images of the Zn foil soaked in electrolyte for 24 hours.

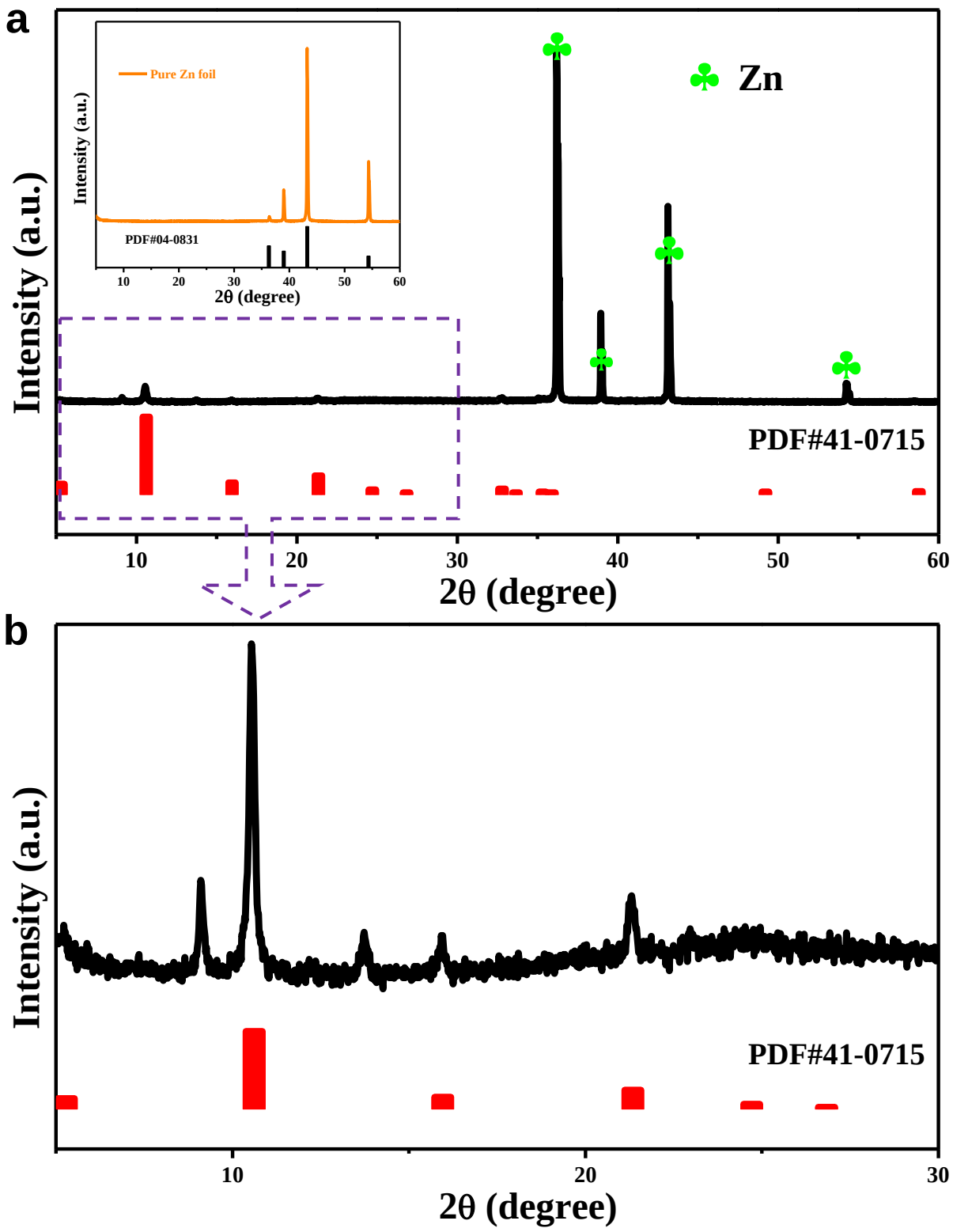

Figure S36. a, b) XRD patterns of the soaked Zn foil. Inset in a) shows the XRD pattern of pure Zn foil.

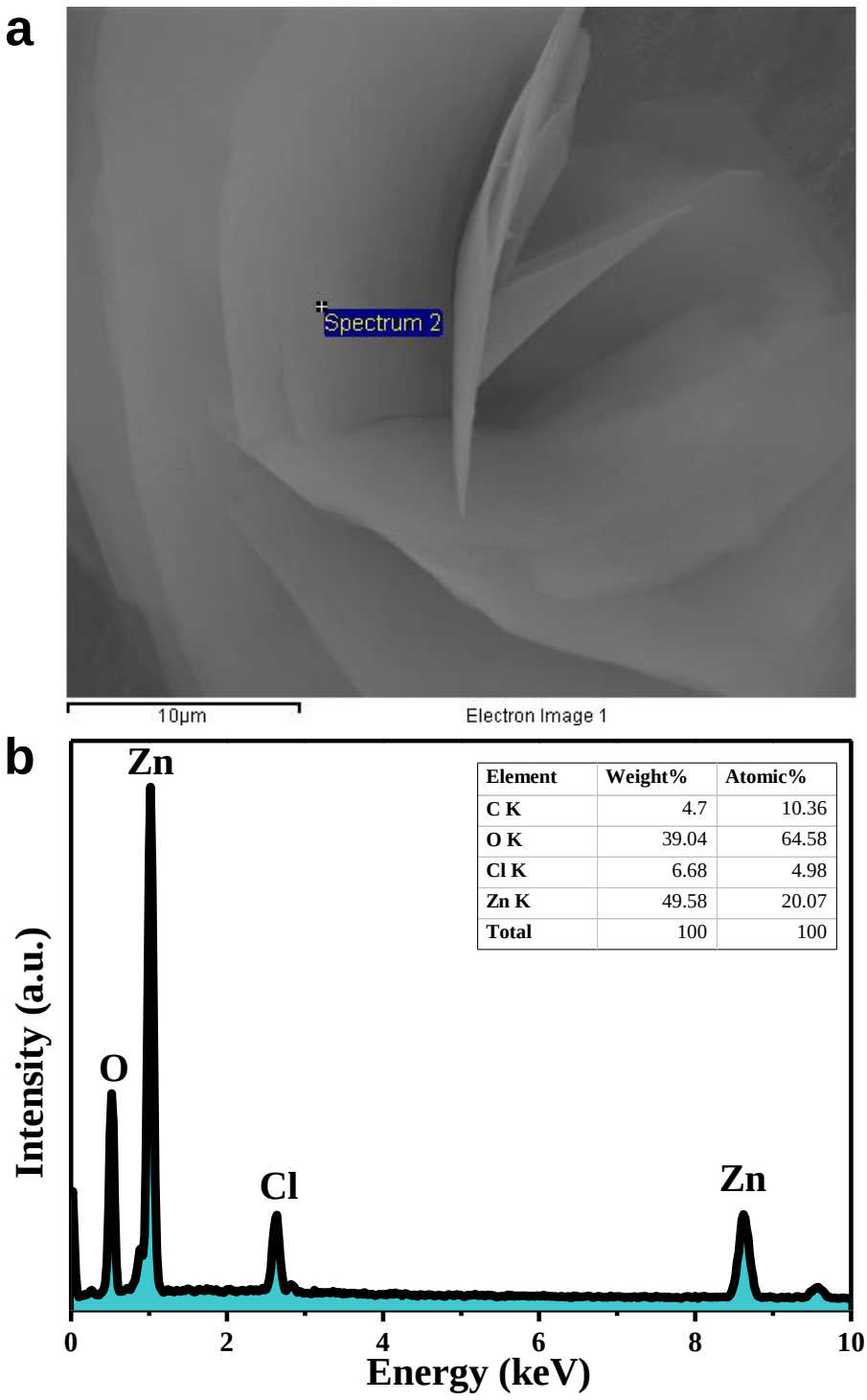

Element	Weight%	Atomic%
C K	4.7	10.36
O K	39.04	64.58
Cl K	6.68	4.98
Zn K	49.58	20.07
Total	100	100

Figure S37. a) SEM image of the BZS sheets. b) EDX spectra obtained at the area marked in a). Inset in b) gives the measured elemental contents.

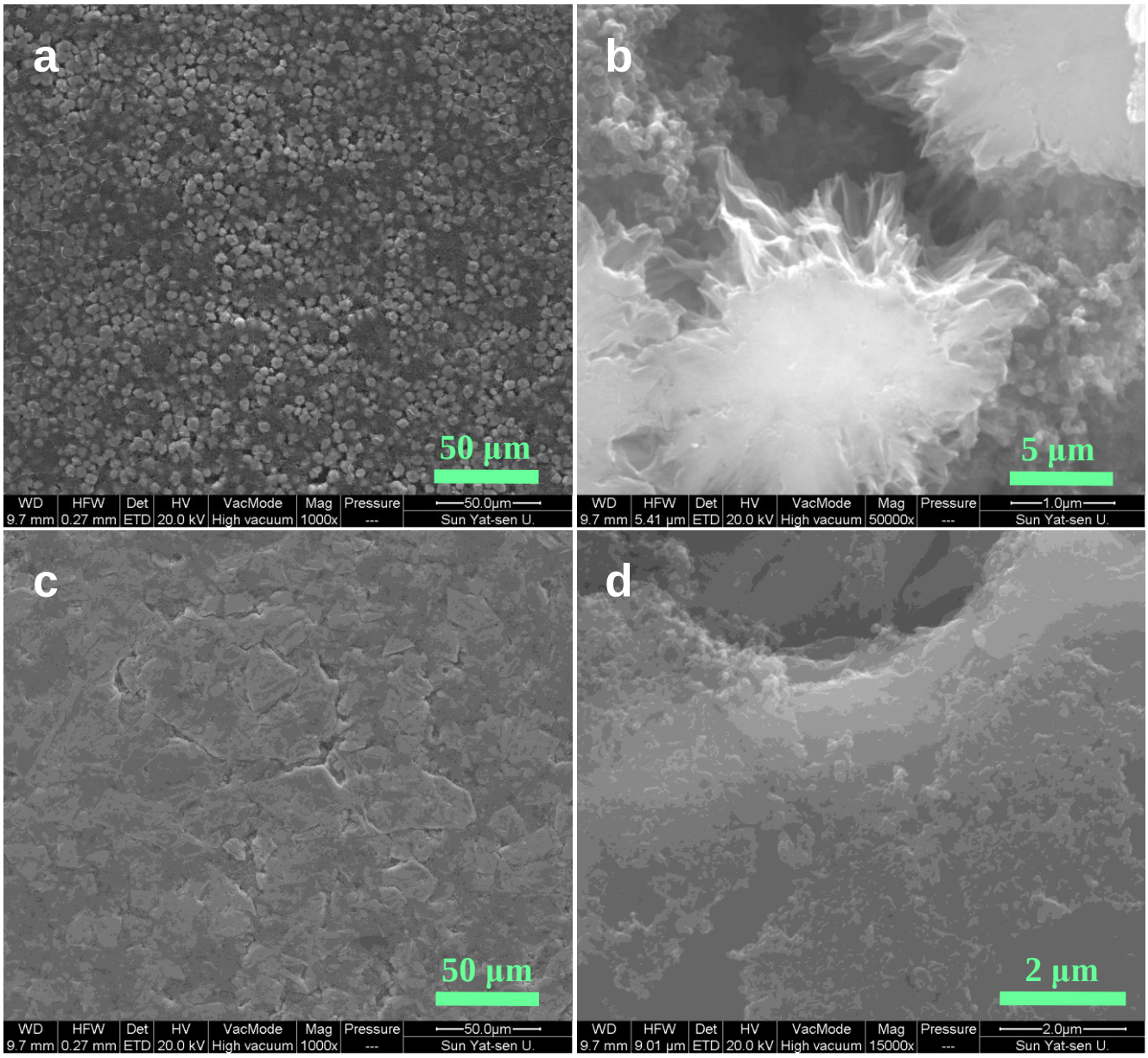

Figure S38. a, b) SEM images of the $H_{11}Al_2V_6O_{23.2}$ electrode obtained after soaking in electrolyte for 24 hours. c, d) SEM images of the $V_5O_{12}{\cdot}6H_2O$ electrode obtained after soaking in electrolyte for 24 hours.

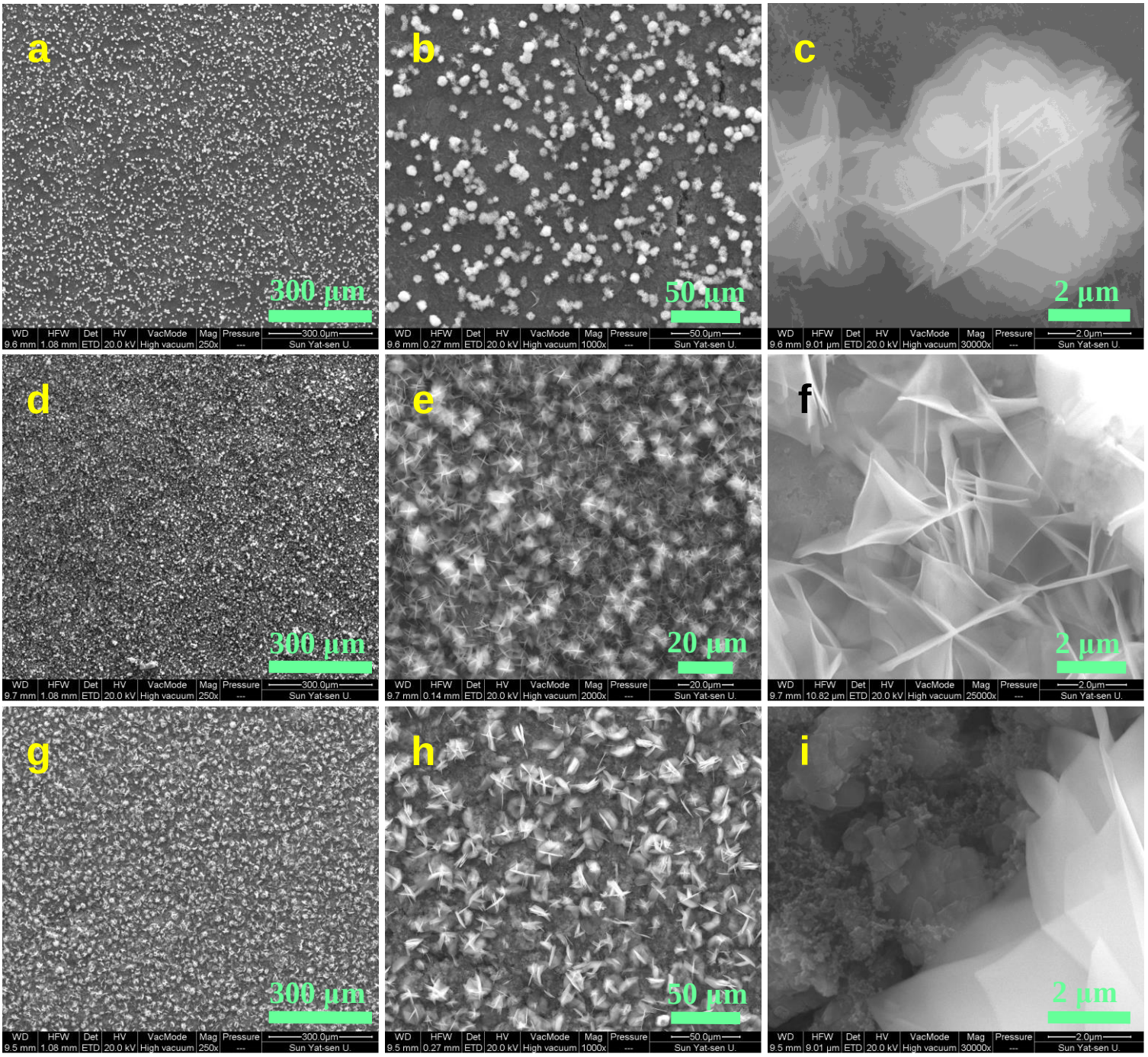

Figure S39. a – c) SEM images of the VO_2 electrode obtained after soaking in electrolyte for 24 hours. d – f) SEM images of the V_2O_5 electrode obtained after soaking in electrolyte for 24 hours. g – i) SEM images of the $K_{0.486}V_2O_5$ electrode obtained after soaking in electrolyte for 24 hours.

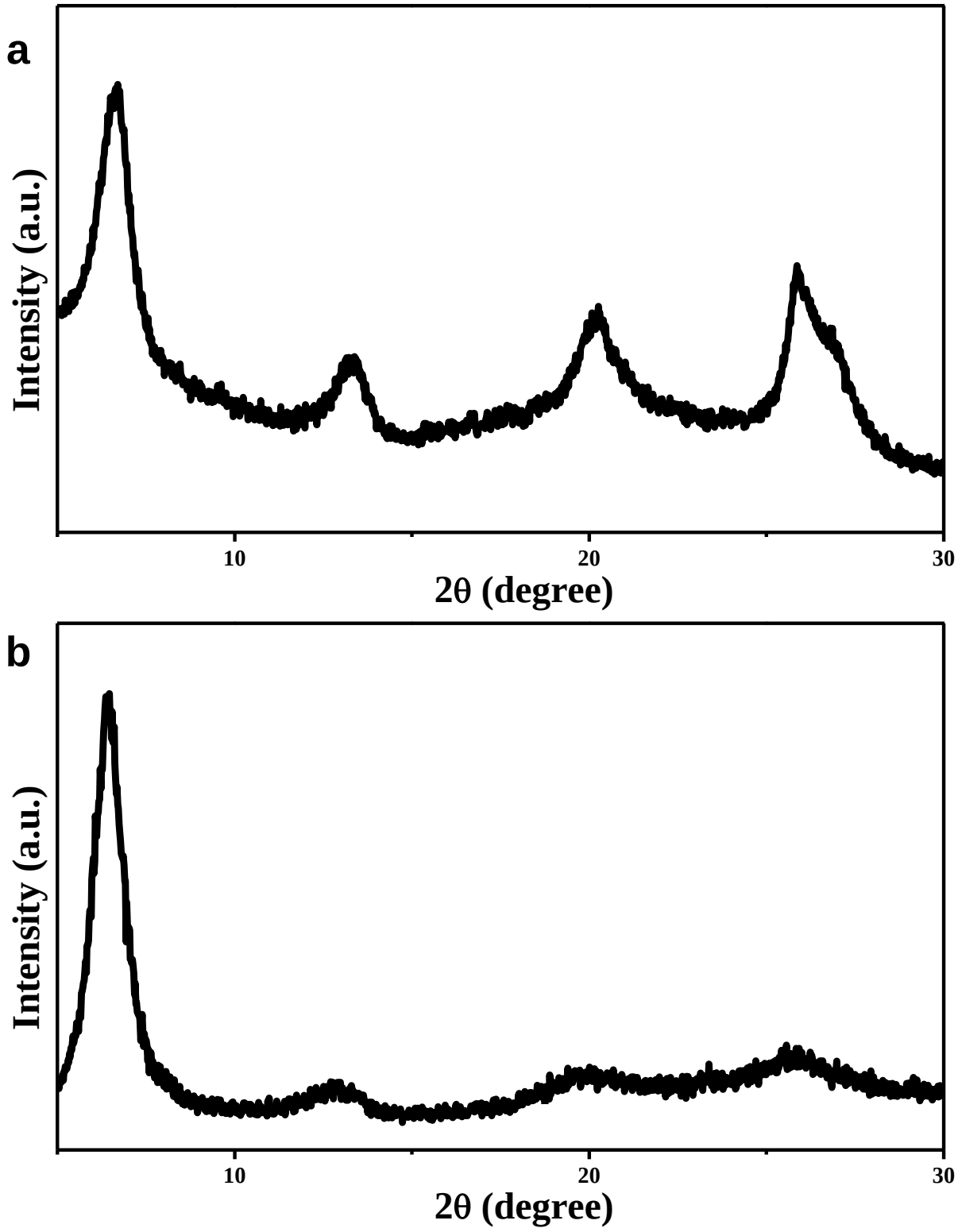

Figure S40. XRD patterns of the electrodes obtained after soaking in electrolyte for 24 hours: a) $H_{11}Al_2V_6O_{23.2}$; b) $V_5O_{12}{\cdot}6H_2O$.

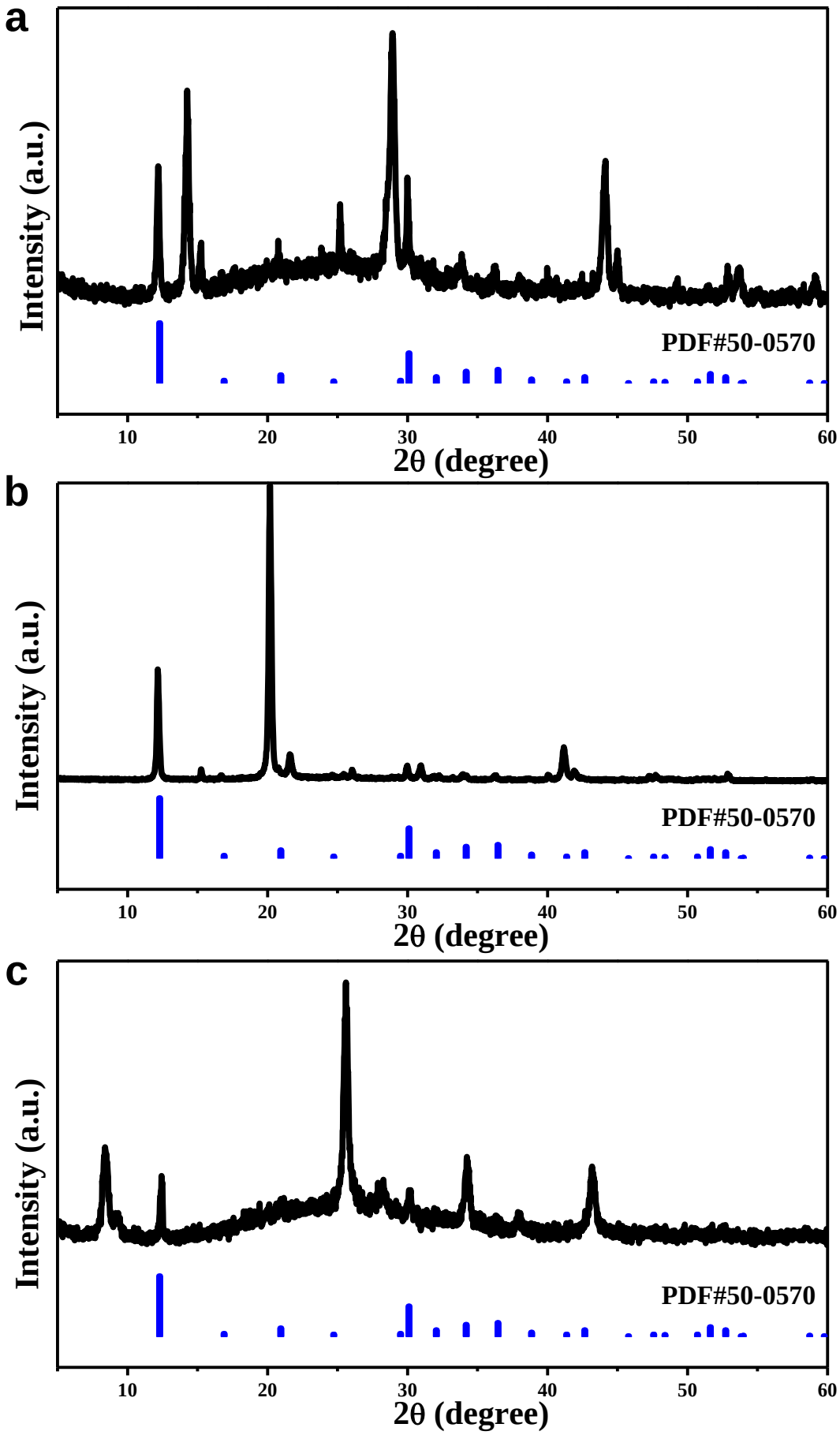

Figure S41. XRD patterns of the electrodes obtained after soaking in electrolyte for 24 hours: a) VO_2; b) V_2O_5; c) $K_{0.486}V_2O_5$.

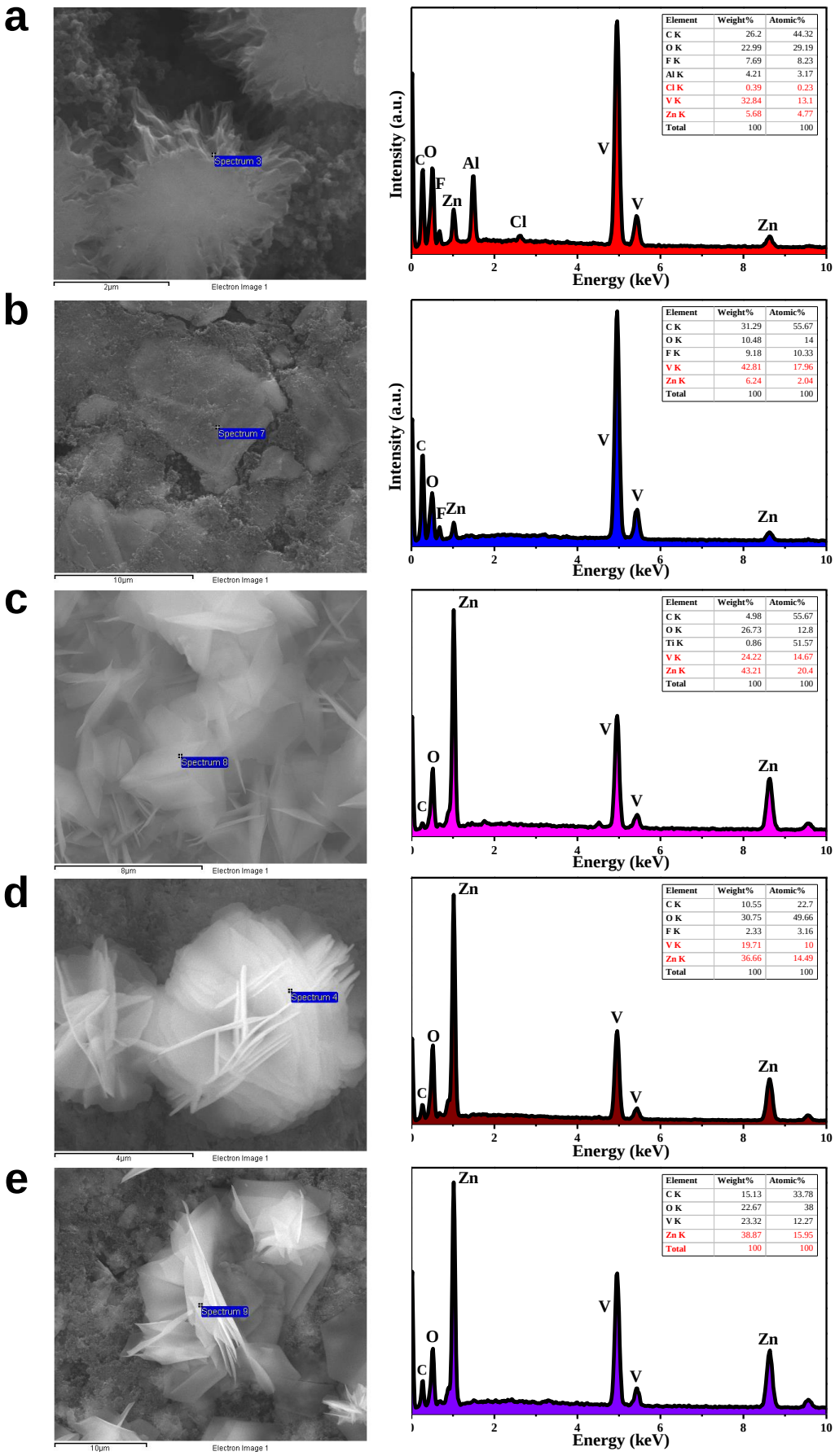

Figure S42. EDX results of the electrodes obtained after soaking in electrolyte for 24 hours: a) $H_{11}Al_2V_6O_{23.2}$; b) $V_5O_{12}\cdot 6H_2O$; c) VO_2; d) V_2O_5; e) $K_{0.486}V_2O_5$.

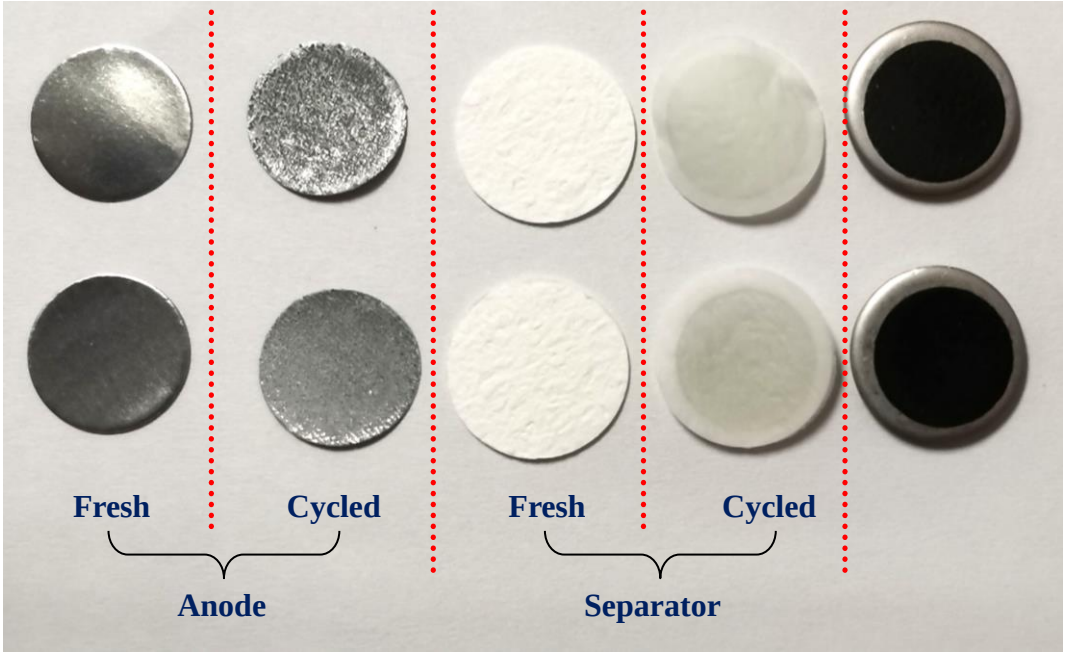

Figure S43. Optical image of the cycled button cells obtained at different current densities (Top: high current; Bottom: low current). It can clearly see the roughened Zn foil and the colored separator, which suggest the dissolution of electrode material ($H_{11}Al_2V_6O_{23.2}$) in the aqueous electrolyte.

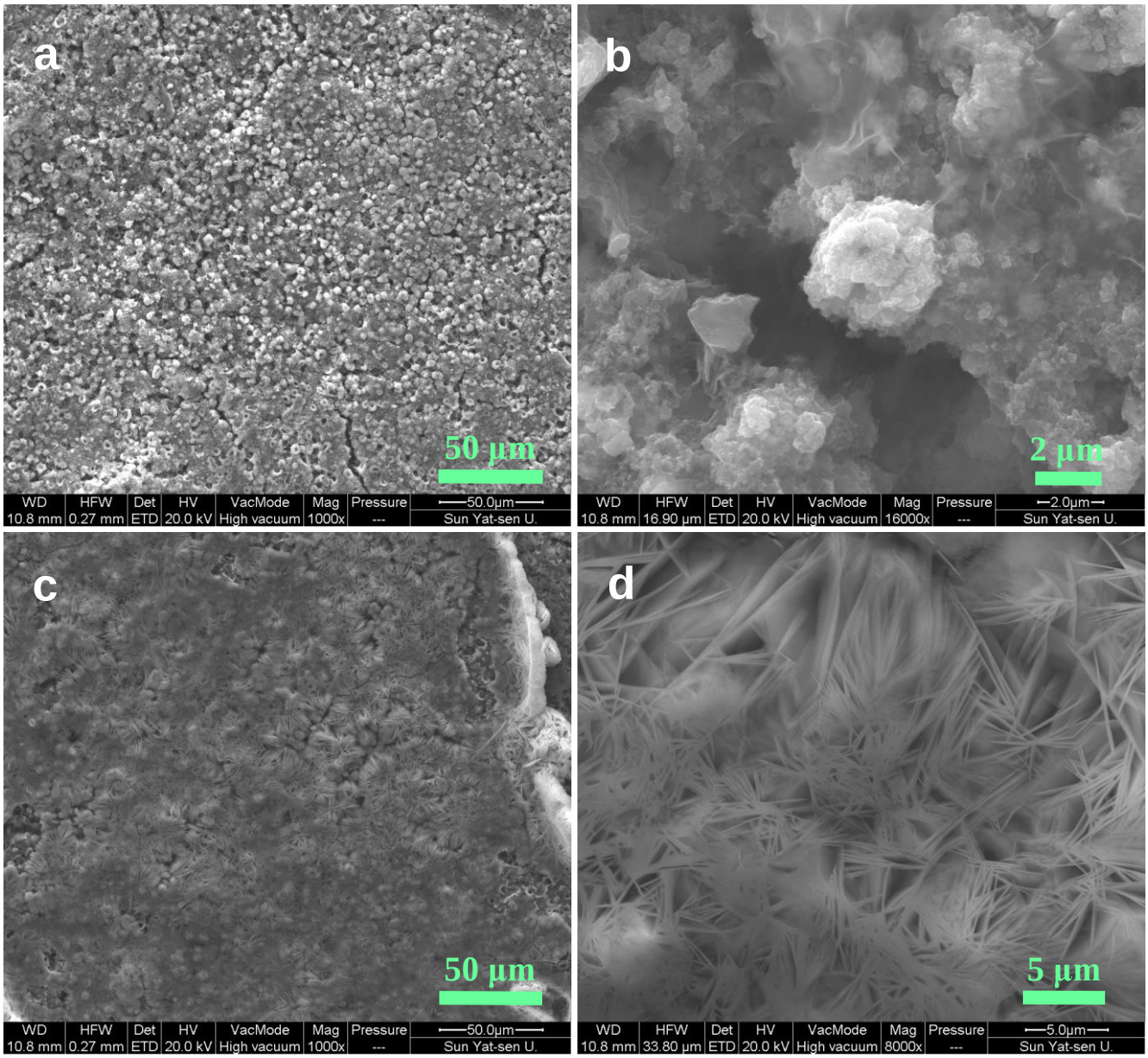

Figure S44. SEM images of the $H_{11}Al_2V_6O_{23.2}$ electrodes obtained at fully charged state after discharging/charging for 1000 cycles at 5 A g^{-1} in different electrolytes: a, b) 2M $Zn(ClO_4)_2$ in H_2O/PC (1:1 by volume); c, d) 2M $Zn(ClO_4)_2$ aqueous solution.

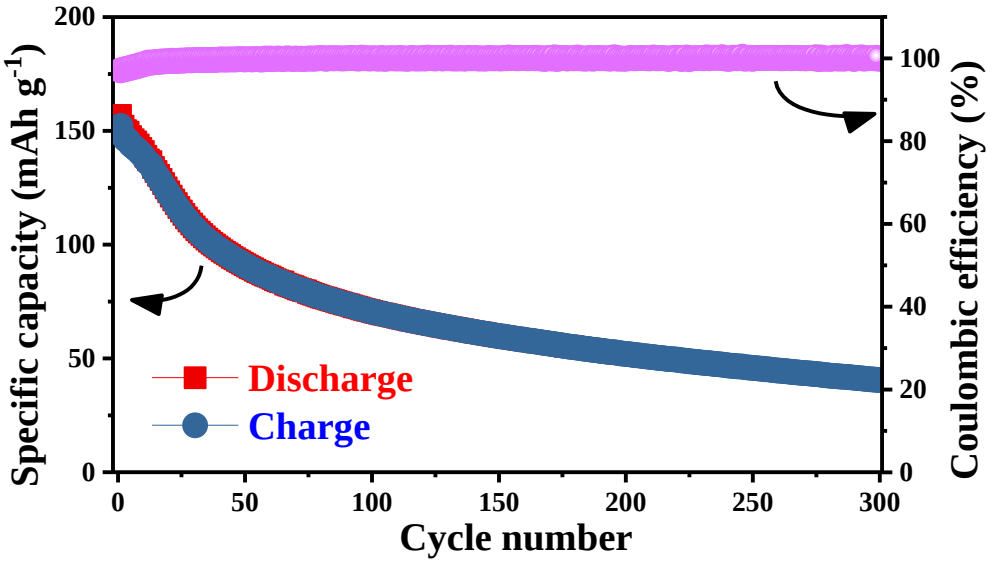

Figure S45. The cycling performance of the AVO electrodes at 0.02 A g^{-1} in PC/H_2O-$Zn(ClO_4)_2$ electrolyte.

REFERENCES

1. Kundu, D.; Adams, B. D.; Duffort, V.; Vajargah, S. H.; Nazar, L. F. A High-Capacity and Long-Life Aqueous Rechargeable Zinc Battery Using a Metal Oxide Intercalation Cathode. *Nat. Energy* **2016**, 1, 16119.
2. Jo, J. H.; Sun, Y-K.; Myung, S-T. Hollandite-Type Al-Doped $VO_{1.52}(OH)_{0.77}$ as a Zinc Ion Insertion Host Material. *J. Mater. Chem. A* **2017**, 5, 8367–8375.
3. Hu, P.; Yan, M.; Zhu, T.; Wang, X.; Wei, X.; Li, J.; Zhou, L.; Li, Z.; Chen, L.; Mai, L. Zn/V_2O_5 Aqueous Hybrid-Ion Battery with High Voltage Platform and Long Cycle Life. *ACS Appl. Mater. Interfaces* **2017**, 9, 42717–42722.
4. Yan, M.; He, P.; Chen, Y.; Wang, S.; Wei, Q.; Zhao, K.; Xu, X.; An, Q.; Shuang, Y.; Shao, Y.; Mueller, K. T.; Mai, L.; Liu, J.; Yang, J. Water-Lubricated Intercalation in $V_2O_5{\cdot}nH_2O$ for High-Capacity and High-Rate Aqueous Rechargeable Zinc Batteries. *Adv. Mater.* **2017**, 1703725.
5. He, P.; Quan, Y.; Xu, X.; Yan, M.; Yang, W.; An, Q.; He, L.; Mai, L. High-Performance Aqueous Zinc-Ion Battery Based on Layered $H_2V_3O_8$ Nanowire Cathode. *Small* **2017**, 1702551.
6. Sambandam, B.; Soundharrajan, V.; Kim, S.; Alfaruqi, M. H.; Jo, J.; Kim, S.; Mathew, V.; Sun, Y-K.; Kim, J. Aqueous Rechargeable Zn-Ion Batteries: An Imperishable and High-Energy $Zn_2V_2O_7$ Nanowire Cathode through Intercalation Regulation. *J. Mater. Chem. A* **2018**, 6, 3850–3856.
7. Xia, C.; Guo, J.; Lei, Y.; Liang, H.; Zhao, C.; Alshareef, H. N. Rechargeable Aqueous Zinc-Ion Battery Based on Porous Framework Zinc Pyrovanadate Intercalation Cathode. *Adv. Mater.* **2017**, 1705580.
8. Soundharrajan, V.; Sambandam, B.; Kim, S.; Alfaruqi, M. H.; Putro, D. Y.; Jo, J.; Kim, S.; Mathew, V.; Sun, Y-K.; Kim, J. $Na_2V_6O_{16}{\cdot}3H_2O$ Barnesite Nanorod: An Open Door to Display a Stable and High Energy for Aqueous Rechargeable Zn-Ion Batteries as Cathodes. *Nano Lett.* **2018**, 18, 2402–2410.
9. Xia, C.; Guo, J.; Li, P.; Zhang, X.; Alshareef, H. N. Highly Stable Aqueous Zinc-Ion Storage Using a Layered Calcium Vanadium Oxide Bronze Cathode. *Angew. Chem. Int. Ed.* **2018**, 57, 3943–3948.

10. He, P.; Zhang, G.; Liao, X.; Yan, M.; Xu, X.; An, Q.; Liu, J.; Mai, L. Sodium Ion Stabilized Vanadium Oxide Nanowire Cathode for High-Performance Zinc-Ion Batteries. *Adv. Energy Mater.* **2018**, 8, 1702463.
11. Wei, T.; Li, Q.; Yang, G.; Wang, C. An Electrochemically Induced Bilayered Structure Facilitates Long-Life Zinc Storage of Vanadium Dioxide. *J. Mater. Chem. A* **2018**, 6, 8006–8012.
12. Ding, J.; Du, Z.; Gu, L.; Li, B.; Wang, L.; Wang, S.; Gong, Y.; Yang, S. Ultrafast Zn^{2+} Intercalation and Deintercalation in Vanadium Dioxide. *Adv. Mater.* **2018**, 30, 1800762.
13. Hu, P.; Zhu, T.; Wang, X.; Wei, X.; Yan, M.; Li, J.; Luo, W.; Yang, W.; Zhang, W.; Zhou, L.; Zhou, Z.; Mai, L. Highly Durable $Na_2V_6O_{16}\cdot 1.63H_2O$ Nanowire Cathode for Aqueous Zinc-Ion Battery. *Nano Lett.* **2018**, 18, 1758–1763.
14. Cai, Y.; Liu, F.; Luo, Z.; Fang, G.; Zhou, J.; Pan, A.; Liang, S. Pilotaxitic $Na_{1.1}V_3O_{7.9}$ Nanoribbons/Graphene as High-Performance Sodium Ion Battery and Aqueous Zinc Ion Battery Cathode. *Energy Storage Mater.* **2018**, 13, 168–174.
15. Tang, B.; Fang, G.; Zhou, J.; Wang, L.; Lei, Y.; Wang, C.; Lin, T.; Tang, Y.; Liang, S. Potassium Vanadates With Stable Structure and Fast Ion Diffusion Channel as Cathode for Rechargeable Aqueous Zinc-Ion Batteries. *Nano Energy* **2018**, 51, 579–587.
16. Guo, X.; Fang, G.; Zhang, W.; Zhou, J.; Shan, L.; Wang, L.; Wang, C.; Lin, T.; Tang, Y.; Liang, S. Mechanistic Insights of Zn^{2+} Storage in Sodium Vanadates. *Adv. Energy Mater.* **2018**, 8, 1801819.
17. Ming, F.; Liang, H.; Lei, Y.; Kandambeth, S.; Eddaoudi, M.; Alshareef, H. N. Layered $Mg_xV_2O_5\cdot nH_2O$ as Cathode Material for High-Performance Aqueous Zinc Ion Batteries. *ACS Energy Lett.* **2018**, 3, 2602–2609.
18. Park, J.; Jo, J.; Aniskevich, Y.; Bakavets, A.; Ragoisha, G.; Streltsov, E.; Kim, J.; Myung, S-T. Open-Structured Vanadium Dioxide as an Intercalation Host for Zn Ions: Investigation by First-Principles Calculation and Experiments. *Chem. Mater.* **2018**, 30, 6777–6787.

19. Yang, G.; Wei, T.; Wang, C. Self-Healing Lamellar Structure Boosts Highly Stable Zinc-Storage Property of Bilayered Vanadium Oxides. *ACS Appl. Mater. Interfaces* **2018**, 10, 35079–35089.
20. Yang, Y.; Tang, Y.; Fang, G.; Shan, L.; Guo, J.; Zhang, W.; Wang, C.; Wang, L.; Zhou, J.; Liang, S. Li^+ Intercalated $V_2O_5{\cdot}nH_2O$ with Enlarged Layer Spacing and Fast Ion Diffusion as an Aqueous Zinc-Ion Battery Cathode. *Energy Environ. Sci*. **2018**, 11, 3157–3162.
21. Wang, F.; Zhang, L.; Dai, X.; Wang, X.; Niu, Z.; Chen, J. Aqueous Rechargeable Zinc/Sodium Vanadate Batteries with Enhanced Performance from Simultaneous Insertion of Dual Carriers. *Nat. Commun.* **2018**, 9, 1656.
22. Liu, F.; Chen, Z.; Fang, G.; Wang, Z.; Cai, Y.; Tang, B.; Zhou, J.; Liang, S. V_2O_5 Nanospheres with Mixed Vanadium Valences as High Electrochemically Active Aqueous Zinc-Ion Battery Cathode. *Nano-Micro Lett.* **2019**, 11, 98–108.
23. Dai, X.; Wan, F.; Zhang, L.; Cao, H.; Niu, Z. Freestanding Graphene/VO_2 Composite Films for Highly Stable Aqueous Zn-Ion Batteries with Superior Rate Performance. *Energy Storage Mater*. **2019**, 17, 143–150.
24. Tang, B.; Zhou, J.; Fang, G.; Guo, S.; Guo, X.; Shan, L.; Tang, Y.; Liang, S. Structural Modification of V_2O_5 as High-Performance Aqueous Zinc-Ion Battery Cathode. *J. Electrochem. Soc.* **2019**, 166, A480–A486.
25. Zhang, N.; Jia, M.; Dong, Y.; Wang, Y.; Xu, J.; Liu, Y.; Jiao, L.; Cheng, F. Hydrated Layered Vanadium Oxide as a Highly Reversible Cathode for Rechargeable Aqueous Zinc Batteries. *Adv. Funct. Mater*. **2019**, 29, 1807331.
26. Islam, S.; Alfaruqi, M. H.; Sambandam, B.; Putro, D. Y.; Kim, S.; Jo, J.; Kim, S.; Mathew, V.; Kim, J. A New Rechargeable Battery Based on a Zinc Anode and a NaV_6O_{15} Nanorod Cathode. *Chem. Commun*. **2019**, 55, 3793–3796.
27. Shin, J.; Choi, D. S.; Lee, H. J.; Jung, Y.; Choi, Y. W. Hydrated Intercalation for High-Performance Aqueous Zinc Ion Batteries. *Adv. Energy Mater.* **2019**, 9, 1900083.

28. Lan, B.; Peng, Z.; Chen, L.; Tang, C.; Dong, S.; Chen, C.; Zhou, M.; Chen, C.; An, Q.; Luo, P. Metallic Silver Doped Vanadium Pentoxide Cathode for Aqueous Rechargeable Zinc Ion Batteries. *J. Alloy. Compd.* **2019**, 787, 9–16.
29. Li, Z.; Ganapathy, S.; Xu, Y.; Zhou, Z.; Sarilar, M.; Wagemaker, M. Mechanistic Insight into the Electrochemical Performance of Zn/VO_2 Batteries with an Aqueous $ZnSO_4$ Electrolyte. *Adv. Energy Mater.* **2019**, 9, 1900237.
30. Shan, L.; Zhou, J.; Zhang, W.; Xia, C.; Guo, S.; Ma, X.; Fang, G.; Wu, X.; Liang, S. Highly Reversible Phase Transition Endows V_6O_{13} with Enhanced Performance as Aqueous Zinc-Ion Battery Cathode. *Energy Technol.* **2019**, 7, 1900022.
31. Bin, D.; Liu, Y.; Yang, B.; Huang, J.; Dong, X.; Zhang, X.; Wang, Y.; Xia, Y. Engineering a High-Energy-Density and Long Lifespan Aqueous Zinc Battery via Ammonium Vanadium Bronze. *ACS Appl. Mater. Interfaces* **2019**, 11, 20796–20803.
32. Li, Q.; Wei, T.; Ma, K.; Yang, G.; Wang, C. Boosting the Cyclic Stability of Aqueous Zinc-Ion Battery Based on Al-Doped $V_{10}O_{24}{\cdot}12H_2O$ Cathode Materials. *ACS Appl. Mater. Interfaces* **2019**, 11, 20888–20894.
33. Yang, Y.; Tang, Y.; Liang, S.; Wu, Z.; Fang, G.; Cao, X.; Wang, C.; Lin, T.; Pan, A.; Zhou, J. Transition Metal Ion-Preintercalated V_2O_5 as High-Performance Aqueous Zinc-Ion Battery Cathode with Broad Temperature Adaptability. *Nano Energy* **2019**, 61, 617–625.
34. Liu, C.; Neale, Z.; Zheng, J.; Jia, X.; Huang, J.; Yan, M.; Tian, M.; Wang, M.; Yang, J.; Cao, G. Z. Expanded Hydrated Vanadate for High-Performance Aqueous Zinc-Ion Batteries. *Energy Environ. Sci.* **2019**, 12, 2273–2285.
35. Chen, L.; Yang, Z.; Huang, Y. Monoclinic VO_2(D) Hollow Nanospheres with Super-Long Cycle Life for Aqueous Zinc Ion Batteries. *Nanoscale* **2019**, 11, 13032–13039.
36. Wei, T.; Li, Q.; Yang, G.; Wang, C. Pseudo-Zn-Air and Zn-Ion Intercalation Dual Mechanisms to Realize High-Areal Capacitance and Long-Life Energy Storage in Aqueous Zn Battery. *Adv. Energy Mater.* **2019**, 9, 1901480.

37. Zhao, J.; Ren, H.; Liang, Q.; Yuan, D.; Xi, S.; Wu, C.; Manalastas, W.; Ma, J.; Fang, W.; Zheng, Y.; Du, C.; Srinivasan, M.; Yan, Q. High-Performance Flexible Quasi-Solid-State Zinc-Ion Batteries with Layer-Expanded Vanadium Oxide Cathode and Zinc/Stainless Steel Mesh Composite Anode. *Nano Energy* **2019**, 62, 94–102.
38. Zhu, K.; Wu, T.; Huang, K. $NaCa_{0.6}V_6O_{16}\cdot 3H_2O$ as an Ultra-Stable Cathode for Zn-Ion Batteries: The Roles of Pre-Inserted Dual-Cations and Structural Water in V_3O_8 Layer. *Adv. Energy Mater*. **2019**, 9, 1901968.
39. Ghosh, M.; Vijayakumar, V.; Kurungot, S. Dendrite Growth Suppression by Zn^{2+}-Integrated Nafion Ionomer Membranes: Beyond Porous Separators toward Aqueous Zn/V_2O_5 Batteries with Extended Cycle Life. *Energy Technol.* **2019**, 7, 1900442.
40. Zeng, J.; Chao, K.; Wang, W.; Wei, X.; Liu, C.; Peng, H.; Zhang, Z.; Guo, X.; Li, G. Silver Vanadium Oxide@Water-Pillared Vanadium Oxide Coaxial Nanocables for Superior Zinc Ion Storage Properties. *Inorg. Chem. Front.* **2019**, 6, 2339–2348.
41. Zhou, W.; Chen, J.; Chen, M.; Xu, X.; Tian, Q.; Xu, J.; Wong, C-P. Rod-Like Anhydrous V_2O_5 Assembled by Tiny Nanosheets as a High-Performance Cathode Material for Aqueous Zinc-Ion Batteries. *RSC Adv.* **2019**, 9, 30556–30564.
42. Wang, L.; Huang, K.; Chen, J.; Zheng, J. Ultralong Cycle Stability of Aqueous Zinc-Ion Batteries with Zinc Vanadium Oxide Cathodes. *Sci. Adv.* **2019**, 5, eaax4279.
43. Liu, Y.; Li, Q.; Ma, K.; Yang, G.; Wang, C. Graphene Oxide Wrapped CuV_2O_6 Nanobelts as High-Capacity and Long-Life Cathode Materials of Aqueous Zinc-Ion Batteries. *ACS Nano* **2019**, 13, 12081–12089.
44. Chen, X.; Wang, L.; Li, H.; Cheng, F.; Chen, J. Porous V_2O_5 Nanofibers as Cathode Materials for Rechargeable Aqueous Zinc-Ion Batteries. *J. Energy Chem*. **2019**, 38, 20–25.

45. Wang, X.; Ma, L.; Sun, J. Vanadium Pentoxide Nanosheets In-Situ Spaced with Acetylene Black as Cathodes for High-Performance Zinc-lon Batteries. *ACS Appl. Mater. Interfaces* **2019**, 11, 41297–41303.
46. Liao, M.; Wang, J.; Ye, L.; Sun, H.; Wen, Y.; Wang, C.; Sun, X.; Wang, B.; Peng, H. Extraction of Oxygen Anions from Vanadium Oxide Making Deeply Cyclable Aqueous Zinc Ion Battery. *Angew. Chem. Int. Ed*. DOI:10.1002/anie.201912203.
47. Chen, S.; Zhang, Y.; Geng, H.; Yang, Y.; Rui, X.; Li, C. Zinc Ions Pillared Vanadate Cathodes by Chemical Pre-Intercalation Towards Long Cycling Life and Low-Temperature Zinc Ion Batteries. *J. Power Sources* **2019**, 441, 227192.
48. Li, Q.; Liu, Y.; Ma, K.; Yang, G.; Wang, C. In Situ Ag Nanoparticles Reinforced Pseudo-Zn-Air Reaction Boosting $Ag_2V_4O_{11}$ as High-Performance Cathode Material for Aqueous Zinc-Ion Batteries. *Small Methods* **2019**, 3, 1900637.
49. Guo, J.; Ming, J.; Lei, Y.; Zhang, W.; Xia, C.; Cui, Y.; Alshareef, H. N. Artificial Solid Electrolyte Interphase for Suppressing Surface Reactions and Cathode Dissolution in Aqueous Zinc Ion Batteries. *ACS Energy Lett.* **2019**, 4, 2776–2781.